LBNL-2001117

On Carbon Dioxide Injection into Faults and Fracture Zones for Better Characterization of Permeable Flow Paths in Enhanced Geothermal Systems

Final Report

Curtis M. Oldenburg[1], Thomas M. Daley[1], Andrea Borgia[1], Christine Doughty[1], Yoojin Jung[1], Kyung Jae Lee[1]

Rui Zhang[2]

Bilgin Altundas[3], Nikita Chugunov[3]

[1]Energy Geosciences Division
Lawrence Berkeley National Laboratory

[2]School of Geosciences
University of Louisiana, Lafayette

[3]Schlumberger-Doll Research
Cambridge, MA

December 22, 2017

This page left intentionally blank

ACKNOWLEDGMENT

Support for this work was provided by the Office of Energy Efficiency and Renewable Energy, Geothermal Technologies Office (GTO), U.S. Department of Energy. Additional support was provided by the Assistant Secretary for Fossil Energy (DOE), Office of Coal and Power Systems, through the National Energy Technology Laboratory (NETL), by Lawrence Berkeley National Laboratory under Department of Energy Contract No. DE-AC02-05CH11231, and by EDRA. Pre- and post-processing of TOUGH2 simulations is done using a free GMS license provided by Acquaveo™. We thank Sean Porse (GTO) for insightful questions and comments along with efficient management.

DISCLAIMERS

This page left intentionally blank

TABLE OF CONTENTS

1 INTRODUCTION 13
2 MOTIVATION AND BACKGROUND 14
2.1 Introduction 14
2.2 Prior experience with geophysical imaging in faults and fractures 15
2.3 CO_2 properties favoring push-pull 16
3 SIMULATION OF CO_2 INJECTION AND PRODUCTION 17
3.1 Introduction 17
3.2 Methods 17
3.3 Conceptual and numerical model 18
3.4 Results 19
4 WELL LOGGING 23
4.1 Introduction 23
4.2 Methods 23
4.3 Results 23
4.4 Simulations of Neutron Capture 25
4.5 Conclusions 26
5 MODELING OF ACTIVE SEISMIC MONITORING 27
5.1 Introduction 27
5.2 Methods 27
Fundamentals 27
Fluid and Rock Properties 28
5.3 Results 29
Model System 29
Changes in Stiffness 31
Changes in Vp 32
5.4 Conclusions 36
6 PRESSURE TRANSIENT AND SENSITIVITY FOR SINGLE FAULT 37
6.1 Introduction 37
6.2 Methods and Model System 37
6.3 Summary 45
7 SENSITIVITY AND DATA WORTH FOR A DUAL FAULT SYSTEM 45
7.1 Introduction 45
7.2 Model system 46
7.3 Summary 52
8 DISCUSSION 53
9 FUTURE WORK 54

9.1 Field demonstration 54
9.2 Modeling and Simulation 54
9.3 Fault and Fracture Properties 55
9.4 High-Quality Active Seismic Data Acquisition 55
9.5 Integration with waterless (CO_2-based) stimulation 55
10 CONCLUSIONS 55
11 ACKNOWLEDGMENTS 56
12 REFERENCES 57
13 APPENDIX I 63

LIST OF FIGURES

Figure 1-1. Idealized end-member fracture configurations around a vertical well: (a) dense fracture network; (b) sparse fracture network; (c) discrete non-communicating dominant fractures; and (d) discrete communicating dominant fractures. 13

Figure 2-1. (a) Conceptual model of fault zone from Gudmundsson et al. (2002), along with (b) our model system terminology of a fracture and fracture set. 15

Figure 2-2. Seismic response of a fracture zone connecting horizontal well KB-502 and vertical well KB-5 following injection of CO_2 in KB-502. Data show curvature attribute for a time-slice of 3D seismic data. Other fracture zones can also be inferred from the data. 16

Figure 3-1. Model domain for push-pull simulations. Because of symmetry, we only model one-quarter of the actual system. 17

Figure 3-2. Sketch of coordinate system and intersection of injection well and fault zone along with idealized circular CO_2 plume. 18

Figure 3-3. Schematic geologic cross section of the Rhyolite Ridge fault system at Desert Peak-Brady's geothermal field (modified after Faulds and Garside (2003)). In our model we consider only the single fault on the right-hand side. 18

Figure 3-4. Conceptual model and grid for the Desert Peak 2D model. The 2D-fault has slip-plane (10^{-2} m in thickness), gouge (5 m on both side of slip plane), damage zone (10 m on both side of gouge) and intact matrix (10 m on both side of damage zone). The different rocks may change their hydrogeologic parameters if they are a part of the damage zone, gouge, and slip plane. Geology is after Faulds and Garside (2003). (a) no vertical or horizontal exaggeration; (b) 40 times horizontal exaggeration. 20

Figure 3-5. 2D model of CO_2 injection in a "Brady's-type" normal fault with 60° of dip. Fault gouge and slip plane are homogeneous in hydrogeologic properties. Note how the CO_2 plume develops against the hanging wall of the fault not entering the damage zone in the short time of the simulation. Note also the tooth that develops at the top of the plume. a) 1 day, b) 2 days, c) 4 days, d) 6 days, and e) the same results

with no horizontal exaggeration. The inclined red line is made by the injection cells within the fault gouge. 22

Figure 4-1. Wireline well-logging tools showing estimated sensitivity based on the computed dynamic range for effective properties (bulk density, elastic properties, conductivity, and neutron capture cross section) for expected ranges of $S_w = 1 - S_{CO2,}$ salinity, *P*, and *T*. HLDS = Hostile Environment Litho-Density Sonde; HSLT = Hostile Sonic Logging Tool; HIT = Hostile environment Induction imaging Tool; HAPS = Hostile Accelerator Porosity Sonde. 24

Figure 4-2. Wireline well-logging tools showing estimated feasibility for detecting effective property (bulk density, elastic properties, conductivity, and neutron capture cross section) changes in the various domains of the CO_2 push-pull system (matrix, damage zone, fault gouge, and slip plane). HLDS = Hostile Environment Litho-Density Sonde; HSLT = Hostile Sonic Logging Tool; HIT = Hostile environment Induction imaging Tool; HAPS = Hostile Accelerator Porosity Sonde. 25

Figure 4-3. Profiles of simulation results at 6 days from the SNUPAR code using the output of the TOUGH2-ECO2N runs as input. Colored symbols correspond to different sub-vertical profile lines through the system starting at the slip plane (X = 25 m) and moving to the left to X = 19.5 m. The second frame from the left shows a strong time-lapse capture cross-section signal that suggests that CO_2 can be monitored using neutron capture logging in the considered EGS setting. 26

Figure 5-1. Workflow for modeling V_p and V_s as functions of dry and bulk rock properties and fluid properties. 29

Figure 5-2. P-wave velocity model of the conceptual Desert Peak geothermal field. Schematic cross-section of the Rhyolite Ridge fault zone after Faulds et al. (2010b). Only the right-most (ESE) fault is used in the hydrogeologic modeling (white dashed box). 30

Figure 5-3. The fault zone within the white dashed rectangle in Figure 5-2 is elaborated with 20 times width-along-strata exaggeration. The widths of the matrix, the damage zone, the fault gouge, and the slip plane are 10 m, 10 m, 5 m, and 2 cm, respectively, and the vertical depth of the field ranges from 630 to 1435.4 m below ground (cf. Borgia et al., 2017b) 31

Figure 5-4. Changes in C_{11} (GPa) arising from CO_2 saturation in the fault zone as simulated in the push phase shown in Figure 3-5. 32

Figure 5-5. 1D velocity models 3 m from the slip plane into the hanging wall fault gouge. 33

Figure 5-6. (a) shows crosswell survey geometry with the P-wave velocity model; (b) shows the modeled seismogram. 34

Figure 5-7. (a) Crosswell survey geometry with the P-wave velocity model with CO_2 in the gouge of the fault zone; (b) Modeled wavefield from one source at one time (a wavefield snapshot) with labeled reflection events. 35

Figure 5-8. (a) Seismograms of pre- (top) and post- (middle) CO_2 injection after two days and the difference (bottom). (b) Results of reverse-time migration of pre- and post-CO_2 injection seismograms and their difference (bottom). 36

Figure 6-1. 2D model grid: (a) the whole model domain (note that the dark blue triangular areas at the upper left and lower right corner are not part of the actual model domain); (b) the local area around the well; (c) a close-up of the area near the slip plane, showing the fine discretization. 38

Figure 6-2. CO_2 and water flow during the (a) push and (b) pull period. 39

Figure 6-3. Spatial distribution of pressure change in bar (upper row) and gas saturation (lower row) at 1 hr, 1 day, and 4 days of the push and pull periods. Note that the actual grid is rotated clockwise by 30° to make the fault dip 60°; black arrows point in the vertical direction. 41

Figure 6-4. Pressure transient (solid) and gas saturation (dash-dot) at MW_{50m}, MW_{100m}, and MW_{200m} during the push and pull periods. As a reference case, a pressure transient with water as an agent for the push-pull test (ΔP_w at MW_{200m}) is also shown. 42

Figure 6-5. Temporal variation of the scaled sensitivity to material permeabilities: (a) pressure transient and (b) gas saturation. 43

Figure 6-6. Pressure transients for different permeability conditions: (a) fault gouge, (b) damage zone, and (c) matrix. 44

Figure 6-7. Monte Carlo uncertainty propagation analysis: (a) pressure transient and (b) gas saturation. The thick black line shows the base case, and the other thin lines with different colors represent Monte Carlo realizations. 45

Figure 7-1. (a) Conceptual model of the 2D DVGS system. (b) Simplified model for simulating CO_2 push pull in a dual-fault system. 46

Figure 7-2. Grid geometry of the 2D conceptual model domain: (a) entire view, (b) expanded veiw at the junction of the two faults. Note that the horizontal black lines in (a) indicate the boundaries of different lithologic zones shown in Figure 7-1b. 47

Figure 7-3. Reservoir initial conditions: (a) pressure distribution, (b) temperature distribution 48

Figure 7-4. Reservoir profiles after 30 days-push and following 30 days of pull: (a) pressure distribution after push, (b) temperature distribution after push, (c) gas saturation distribution after push, (d) pressure distribution after pull, (e) temperature distribution after pull, (f) gas saturation distribution after pull. Note that in the plots of gas saturation distributions (c) and (f), different extents of the domain (different *X* and *Z* limits) were used relative to those for the pressure and temperature plots. 49

Figure 7-5. Observed pressure as a function of time at three different locations in the main and conjugate faults: (a) Z = -2925 m, (b) Z = -2520 m, (c) Z = -2100 m. 50

Figure 7-6. Observed temperature as a function of time at three different locations in the main and conjugate faults: (a) Z = -2925 m, (b) Z = -2520 m, (c) Z = -2100 m. 50

Figure 7-7. Observed gaseous phase saturation as a function of time at three different locations in the main and conjugate faults: (a) Z = -2925 m, (b) Z = -2520 m, (c) Z = -2100 m 50

Figure 7-8. Data worth values at each observation point: (a) in push phase, (b) in pull phase. The plots of domain were obtained from the profiles of gas saturation distributions after push and pull, respectively. 52

LIST OF TABLES

Table 3-1. Properties of the Brady's system (ρ is density, ϕ is porosity, k is permeability, and Pc is capillary pressure). 19

Table 7-1. Properties of the DVGS (Borgia et al., 2017a, b; Oldenburg et al., 2016). Rock grain density = 2650 $kg \cdot m^{-3}$, pore compressibility = 7.25×10^{-12} Pa^{-1}, rock grain specific heat = 1000 $J \cdot kg^{-1} \cdot K^{-1}$, and formation thermal conductivity = 2.1 $W \cdot m^{-1} \cdot K^{-1}$, respectively. Note that $1/P_0$ is proportional to the square root of the absolute permeability. 48

This page left intentionally blank

ABSTRACT

We report on a modeling project aimed at assessing the utility of using supercritical carbon dioxide ($scCO_2$) injection to enhance fault characterization in geothermal systems. The motivation for the study came from the need to improve characterization of fault and fracture zones for enhanced geothermal systems (EGS). The potential technical feasibility of the idea is supported by theory and a few published papers on field observations that suggest that $scCO_2$ will provide enhanced contrast for monitoring by seismic and well-logging approaches. We extended the workflow to include a $scCO_2$ and water push-pull injection-production sequence to provide well-test information that can inform characterization of fault hydraulic properties.

There are several properties of $scCO_2$ that make it a promising contrast and hydraulic well-test fluid for EGS: (1) $scCO_2$ is much more compressible than water at downhole in situ conditions, creating variations in stiffness moduli and correspondingly in effective seismic velocity of rock containing $scCO_2$; (2) $scCO_2$ is non-wetting and will therefore tend to stay in the fault/fracture plane and fault gouge without entering the fine-grained matrix; (3) $scCO_2$ is less viscous than geothermal brines, facilitating fracture/fault permeation; (4) $scCO_2$ is denser than other gases (like nitrogen or air) decreasing the buoyant rise of the CO_2 plume in (sub-) vertical faults and fractures.

The methods we used in the study included numerical simulations of push-pull CO_2 injection using TOUGH2/ECO2N, including inversion, sensitivity, and data-worth analyses using iTOUGH2. For evaluating well logging in high-temperature systems, we used dynamic range calculations and a proprietary neutron cross-section simulator (SNUPAR). For active seismic monitoring simulation, we used a finite difference code based on the SPICE codes. The prototypical enhanced geothermal system (EGS) site we focused on is based on the Brady's Hot Springs field in the Desert Peak area, Nevada, but we also investigated a conjugate fault system based on Dixie Valley, Nevada.

Results of simulations of CO_2 push-pull injection into a single dipping fault modeled after Desert Peak show that CO_2 migrates upward in the fault gouge against the hanging wall and does not enter the damage zone because $scCO_2$ is non-wetting relative to the liquid phase. Slip-plane permeability can facilitate upward CO_2 flow and further saturation of the fault gouge. During the pull phase, mostly water is produced because upward buoyancy puts the CO_2 out of reach of fluid production by the well. Therefore the CO_2 push-pull becomes a CO_2 push followed by water pull; this can increase the utility of the method for characterizing fault properties based on pressure-transient analysis because of the use of two fluids (CO_2 and water) with different thermodynamic properties (density, viscosity, compressibility, etc.).

Dynamic range and effective medium modeling of various high-temperature well-logging tools suggests that neutron capture is the most promising approach in the cased-hole environment provided there is enough salinity contrast, e.g., as could be facilitated by pre-flush with high-salinity brine.

Using the simulated pressures and saturations of CO_2 and brine in the fault gouge, we modeled time-lapse surface seismic and borehole seismic with receivers in a vertical seismic profiling

(VSP) geometry, and crosswell seismic monitoring with sources and receivers in boreholes straddling the fault. For the single dipping fault scenario at Desert Peak, our modeling suggests that surface seismic monitoring data would be difficult to invert for fault properties because of the expected weak contrast in seismic signal between pre- and post-CO_2 injection states. In contrast, the crosswell geometry and associated higher frequency content suggest an improved feasibility of detection for the expected time-lapse differences of 1-10% resulting from CO_2 saturation in the fault gouge.

Pressure transient analysis during CO_2 injection and (mostly) water withdrawal provides complementary information on fault zone flow properties. The pressure transient of CO_2 injection into a single fault shows unique traits due to the multiphase flow conditions developed by CO_2 injection. Fault gouge permeability can be estimated from pressure transient data. CO_2 injection into a conjugate fault results in CO_2 entering both limbs of the fault, with CO_2 migration and pressure dissipation in the faults controlled by the permeability of surrounding damage and matrix components of the system.

In summary, modeling and simulation of CO_2 push-pull hydraulic well testing, well logging, and crosswell active seismic monitoring suggest that these approaches are complementary and capable of providing useful characterization information for fault zones in EGS systems. Future work should be directed at more detailed simulations including three-dimensional (3D) simulations, better characterization of changes in rock properties as a function of CO_2 saturation changes, better understanding and characterization of fault and fracture zones so that more realistic modeling can be carried out, and design of very high quality active seismic data collection (low-noise) deployments for EGS systems.

1 INTRODUCTION

Faults and fractures, either natural or a result of stimulation, are needed to provide permeability for sustainable geothermal energy production from high-temperature liquid-dominated geothermal systems in crystalline rocks. But one or two large fractures or faults may dominate fluid production and thereby provide poor thermal sweep through the geothermal resource. Shown in Figure 1-1 are four different end-member configurations of fractures that could be encountered in the natural state or after stimulation to create an Enhanced Geothermal System (EGS). The fracture pattern and properties shown in Figure 1-1a may provide a sustainable geothermal fluid production, while those in Figures 1-1b-d may be controlled by just one or two fractures and lead to inefficient and unsustainable extraction of thermal energy from the resource. In the cases where one major fault or large fracture dominates the flow, stimulation may be needed to create a more pervasive network of fractures to access the entire volume of hot rock.

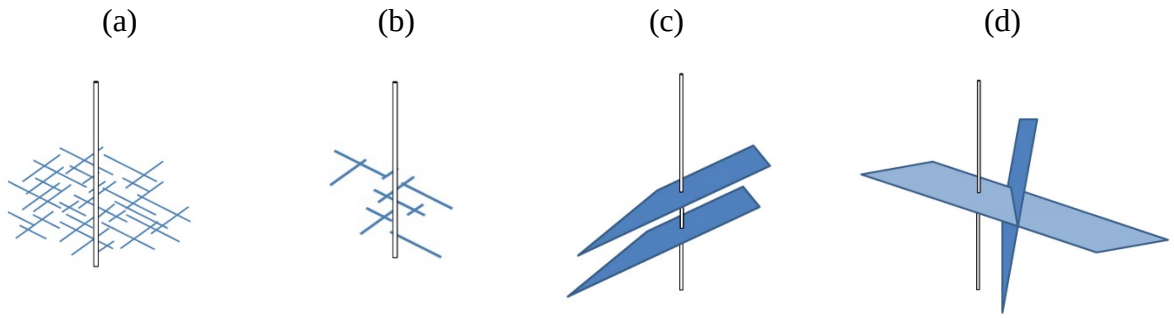

Figure 1-1. Idealized end-member fracture configurations around a vertical well: (a) dense fracture network; (b) sparse fracture network; (c) discrete non-communicating dominant fractures; and (d) discrete communicating dominant fractures.

In order to design fracture stimulation or to evaluate existing fractures and faults in high-temperature EGS reservoirs, effective fracture and fault characterization is needed for both the natural and stimulated faults and fractures. In this report, we summarize our work on evaluating the use of CO_2 injection into faults and fractures as a way of improving EGS reservoir characterization. The idea is that CO_2 injected into faults and fractures will create a detectable contrast for active seismic and well-logging imaging, while also providing a pressure-transient response. Monitoring data collected before, during, and after push-pull can be processed and analyzed to enhance the characterization of the fracture or fault system relative to what is possible without injection of CO_2.

Our approach to developing and testing this idea is based on modeling and simulation of the integration of a suite of monitoring approaches that could be applied to a push-pull injection of CO_2 into faults or fractures. The approach begins with simulation of the push-pull injection of CO_2 into a generic fault or fracture and modeling of the hydraulic pressure-transient analysis. Next we will simulate active seismic monitoring of the CO_2-filled fractures or faults along with wireline well-logging approaches. These hydraulic and geophysical monitoring data will ultimately be used to derive likely configurations and properties of the fault or fracture system.

As stated above, connected fractures and/or faults and associated permeability are essential in any geothermal field to provide surfaces for adequate heat transfer and sufficient fluid

production rates. In many fields, fluid production is sustained by a small number of more prominent fractures and faults. Faults are obviously the best candidate for enhanced fluid production because they tend to have greater extent and permeability. At EGS sites, stimulation of fractures is also done to allow hydraulic connection between the producing well and larger conductive faults (Genter et al., 2010). Therefore, strategies for reservoir development and stimulation will certainly benefit from enhanced fracture and fault network geometric and fluid-dynamic characterization.

To achieve this characterization, we propose to inject and produce supercritical CO_2 ($scCO_2$) in and out of faults, using push-pull (injection/production) well operations, and to use active-source geophysical monitoring and well logging that are sensitive to CO_2 saturation to enhance characterization of the fault zone. The key idea is to use CO_2 to effectively increase the contrast in geophysical properties between fractures or fault zone materials and the matrix rock, improving characterization of the permeable features.

In this report, we summarize briefly the research we carried out to test the technical feasibility of a workflow involving CO_2 injection in a push-pull manner into a fault in an EGS site in order to enhance the characterization of the fault zone. In the workflow, well logging and active seismic monitoring complement one another, and are themselves complemented by pressure-transient and data-worth analysis to inform monitoring locations and measurements to be made that can provide the most value in characterizing the fault during the push-pull process. Greater detail on each of the elements of the workflow can be obtained from our existing publications (Borgia et al. 2015; 2017a, b); Oldenburg et al., 2016) and from manuscripts that are currently either in review or in preparation (Jung et al., submitted; Lee et al. submitted; Zhang et al., in prep.).

2 MOTIVATION AND BACKGROUND

2.1 Introduction

Geothermal energy production from EGS requires the availability of permeability which is normally provided by faults or fracture systems with a variety of possible forms (e.g., Figure 1-1). Many potential EGS sites are in extensional tectonic environments and have poorly connected vertical faults and fractures (e.g., Faulds et al., 2010a, b; Lutz et al., 2009; Genter et al., 2010), a configuration we call topology X (or Y) because the faults and fractures tend generally to be perpendicular to the horizontal (*x*- or *y*-axes). We have adopted parallel faults as the generic model system for our demonstration of the CO_2 push-pull characterization workflow.

Slip along a vertical fault plane usually produces a complex fault structure containing up-to-many-meter-thick fault gouge, one or more slip-planes within the gouge, and a damage zone outside the fault gouge characterized by tensional cracks extending into unfractured rock (the matrix). The relevant properties of fault and fracture sets are the size, shape, aperture, roughness, orientation relative to gravity, gouge thickness, damage-zone thickness, density of secondary fractures, tension shears, and the fracture spacing. These features are shown in Figure 2-1a along with our model conceptualization and nomenclature (Figure 2-1b). While fractures lack a gouge zone, for the purposes of the push-pull characterization approach presented here, faults and fractures are lumped together and our approach is applicable to better characterization of either faults or fractures or both.

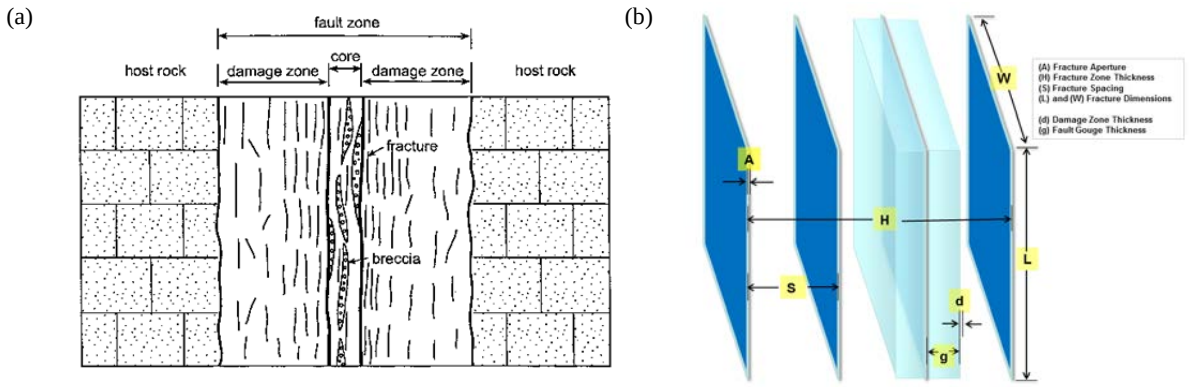

Figure 2-1. (a) Conceptual model of fault zone from Gudmundsson et al. (2002), along with (b) our model system terminology of a fracture and fracture set.

Despite the critical need for fault or fracture zones for providing the necessary permeability pathways for EGS, our ability to image and characterize faults and fractures is very limited at EGS sites. The reason for this is that geothermal brine-filled faults and fractures do not create a strong geophysical contrast relative to matrix in geothermal systems. What is needed is a better way to image and characterize both natural and stimulated fracture and fault permeability at EGS sites.

2.2 Prior experience with geophysical imaging in faults and fractures

Majer et al. (1997) injected air into shallow fractured limestone and observed enhancement in crosswell seismic imaging of the fractures due to the contrast in seismic properties of the gas-filled fractures relative to water-filled. Tura et al. (2013) observed that including gas as the fracture fluid fill enhanced the 4D signal compared to a water-filled fractured. These field studies largely confirm the theory that P-wave velocities change depending on whether pores are filled with gas or water. The use of CO_2 for enhanced imaging was inspired by the results from the In Salah geologic carbon sequestration project in which CO_2 migrating in a fracture zone between injection well KB-502 and well KB-5 was imaged by surface seismic monitoring as shown in Figure 2-2 from Zhang et al. (2015).

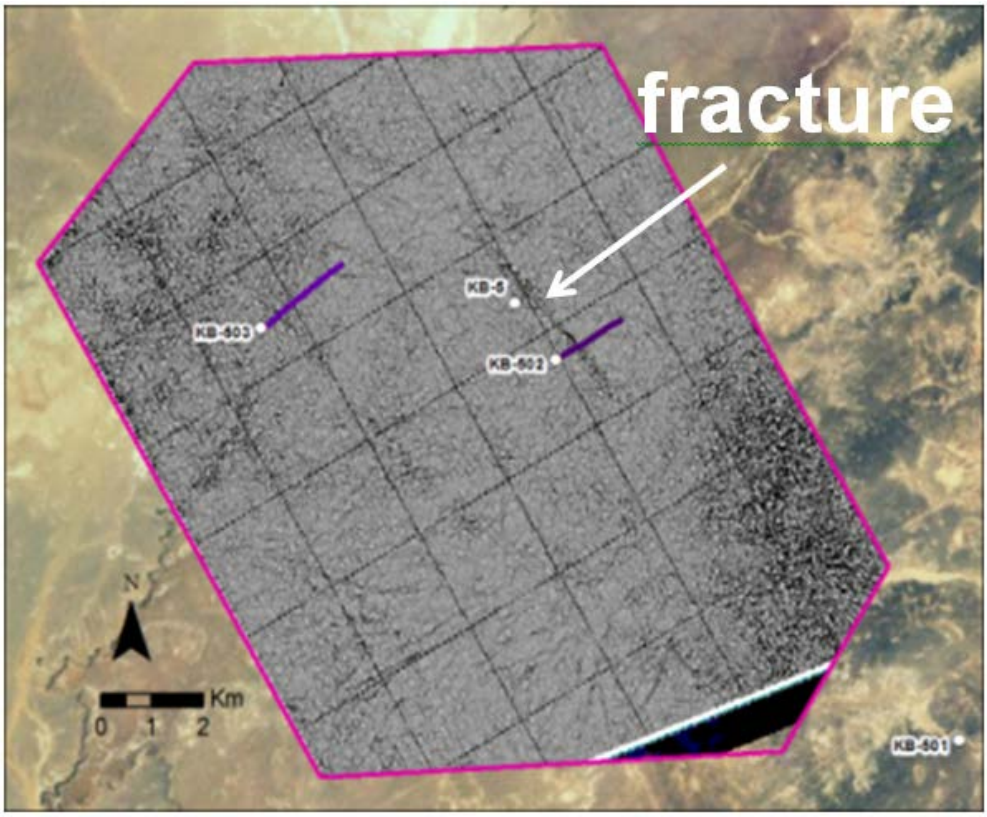

Figure 2-2. Seismic response of a fracture zone connecting horizontal well KB-502 and vertical well KB-5 following injection of CO_2 in KB-502. Data show curvature attribute for a time-slice of 3D seismic data. Other fracture zones can also be inferred from the data.

2.3 CO_2 properties favoring push-pull

The reasons that $scCO_2$ is promising as an injectate to enhance geophysical contrast of faults and fractures are:

(1) $scCO_2$ is much more compressible than water at supercritical conditions, creating variations in stiffness tensor components and resulting seismic velocity;

(2) $scCO_2$ is non-wetting and will therefore tend to stay in the fault gouge or slip plane without entering the fine-grained matrix;

(3) $scCO_2$ is less viscous than ambient brine, facilitating fracture/fault permeation.

(4) $scCO_2$ is denser than other gases (such as nitrogen or air) decreasing the buoyant rise of the CO_2 plume in vertical faults and fractures and thereby enabling a wider permeation of the fault and eventually better recovery during the pull phase.

Theory and observation both strongly suggest that $scCO_2$ injected into a fault zone or fracture zone should enhance the ability to image the CO_2-filled pore space, and thereby better

characterize the permeable feature. In this study, we carried out a simulation- and modeling-based study to test the technical feasibility of this approach for EGS sites.

3 SIMULATION OF CO_2 INJECTION AND PRODUCTION

3.1 Introduction

Simulation of CO_2 injection and production provides the fundamental synthetic data needed to evaluate effectiveness of well logging and active seismic methods for enhancing the characterization of faults and fracture zones. The same simulation approaches described below are used in the pressure-transient, sensitivity, and data-worth analyses. In this section, we summarize the methods and one set of results of the 2D simulation of CO_2 push-pull into a prototypical fault at an EGS site.

3.2 Methods

Simulations of the push-pull injection and production of CO_2 are carried out using TOUGH2/ECO2N (Pruess et al., 2012; Pan et al., 2016), a module that utilizes the CO_2 equation of state from 10 to 300 °C and up to 60 MPa. As an example, the three-dimensional (3D) model domain we used for simulating CO_2 push-pull is shown in Figure 3-1 with model dimensions and the symmetry of the system, which allows us to model only one-quarter of the full system. We use a discretization with grid blocks of size 20 m × y × 20 m, where y = 10^{-4} m in the slip-plane, and 10^{-3}, 10^{-2}, 10^{-1}, and ~1 m in the fault gouge, 10^{-1} m in the damage zone, and ~1 m, and ~10 m in the matrix. The fracture is assumed to be between 2-3 km depth with geothermal gradient of 40 °C/km, fully saturated by brine with salt mass fraction equal to 0.1 at hydrostatic pressure. A conceptual sketch illustrating a vertical well intersecting a dipping fault with idealized CO_2 plume in the fault zone is shown in Figure 3-2. The boundary for the model domain is assumed closed to fluid flow at the top and open to fluid flow on the sides and at the bottom. Additional numerical simulation parameters are given in Table 3-1. Results for this model system were presented in Borgia et al. (2017b).

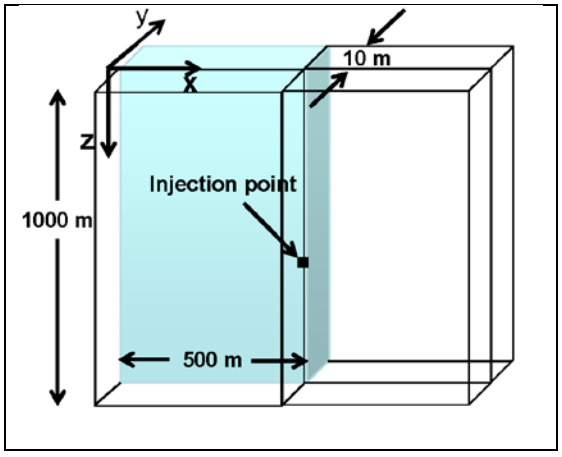

Figure 3-1. Model domain for push-pull simulations. Because of symmetry, we only model one-quarter of the actual system.

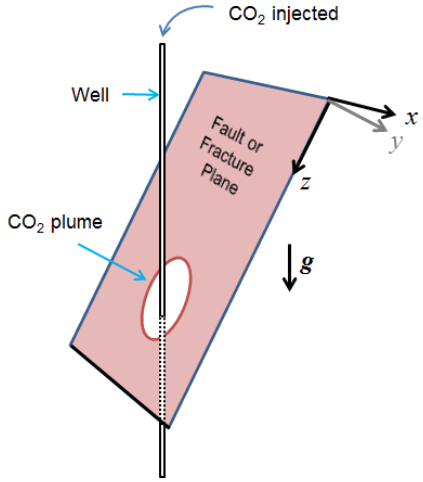

Figure 3-2. Sketch of 3D coordinate system and intersection of injection well and fault zone along with idealized circular CO_2 plume.

3.3 Conceptual and numerical model

In the simplest configuration, we use a two-dimensional (2D) hydrogeologic fault model in order to evaluate the 2D behavior of $scCO_2$ injection and production processes. Our 2D "Brady's type" conceptual fault model consists of a normal fault with a 60° dip (Figure 3-3). The fault has a fault gouge, with a slip-plane within it, and a damage zone on both sides of the fault gouge. Farther away is the unfractured rock matrix (Figure 3-3).

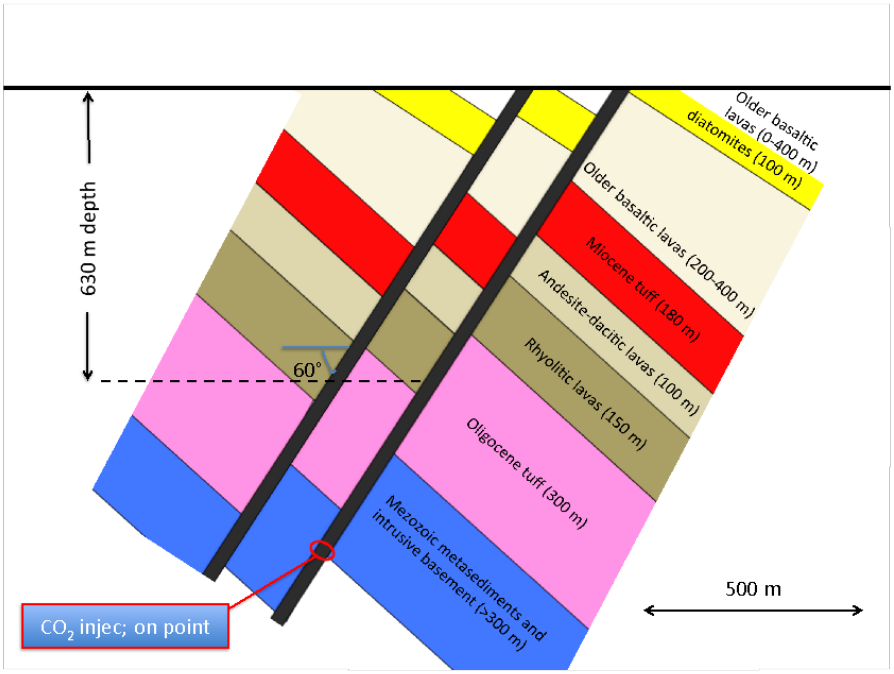

Figure 3-3. Schematic geologic cross section of the Rhyolite Ridge fault system at Desert Peak-Brady's geothermal field (modified after Faulds and Garside (2003)). In our model we consider only the single fault on the right-hand side.

We model the various matrix rocks and include variations in properties of these formations depending on their locations in the damage zone or fault gouge. In the example 2D numerical experiment shown here, we use homogeneous permeability for the cap rock and the reservoir matrix. Formation porosity and density are a function of rock type as shown in Table 3-1. Two-phase relative permeability is modeled after Corey (1954), while we use the van Genuchten (1980) model for capillary pressure curve (*Pc*).

Table 3-1. Properties of the Brady's system (ρ is density, ϕ is porosity, k is permeability, and Pc is capillary pressure).

Hydrogeologic property	ρ (kg/m^3)	ϕ	$k_{x,z}$ (m^2)	Pc (Pa)
High Permeability aquifer				
Matrix (Ryolitic Lavas):	2650	0.1	1.00E-16	1.00E+08
Damage zone:	2650	0.05	1.00E-15	1.00E+08
Fault gouge:	2650	0.1	1.00E-12	0
Slip plane:	2650	0.3	1.00E-12	0
Low Permeability Cover				
Matrix (Oligocente Tuff):	2450	0.1	1.00E-16	1.00E+08
Damage zone:	2550	0.05	1.00E-15	1.00E+08
Fault gouge:	2550	0.1	1.00E-12	0
Slip plane:	2550	0.3	1.00E-12	0
High Permeability Reservoir				
Matrix (Meta Sediments):	2550	0.05	1.00E-16	1.00E+08
Damage zone:	2650	0.05	1.00E-15	1.00E+08
Fault gouge:	2650	0.1	1.00E-12	0
Slip plane:	2650	0.3	1.00E-12	0
Low Permeability Basement				
Matrix (Intrusive Basement):	2750	0.01	1.00E-19	1.00E+08
Damage zone:	2750	0.05	1.00E-15	1.00E+08
Fault gouge:	2750	0.1	1.00E-12	0
Slip plane:	2750	0.3	1.00E-12	0

3.4 Results

We present for brevity one of the many numerical experiments that we have carried out for the 2D Desert Peak system ("Brady's–type" model). The example case consists of a homogeneous fault gouge with larger permeability and smaller capillary pressure than the damage zone. In the numerical experiment, we inject scCO_2 over the full thickness of the fault gouge at a location approximately 2/3 of the distance from the top of the model by setting an invariant 100% CO_2 saturation at pressure 0.3 MPa above the hydrostatic pressure and at the local temperature.

Figure 3-4 shows the discretization and assignment of rock types. Our grid is made of 10 m × 10 m elements in the across-fault (x) and down-dip (z) directions. The water table is assumed to be at -30 m from the ground surface. In the x-direction cell dimensions vary from 10 m in the matrix, to 5 and 1 m in the damage zone, to 1 m and then down to 1 cm in the fault gouge, and finally to 1 cm in the slip plane (Figure 3-4b). The top and bottom boundaries are open to flow.

(a)

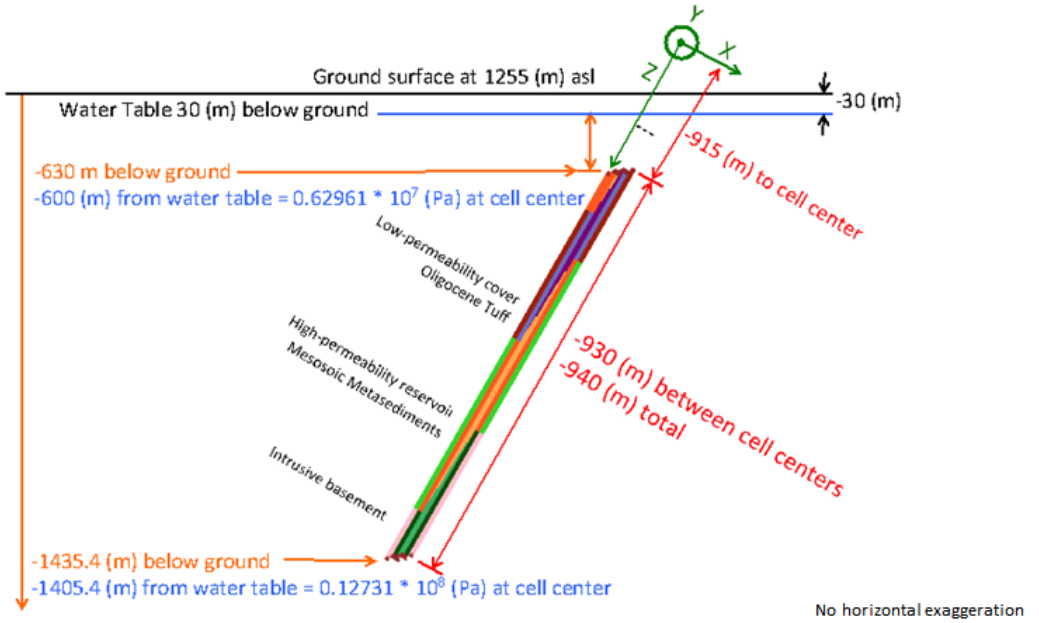

(b)

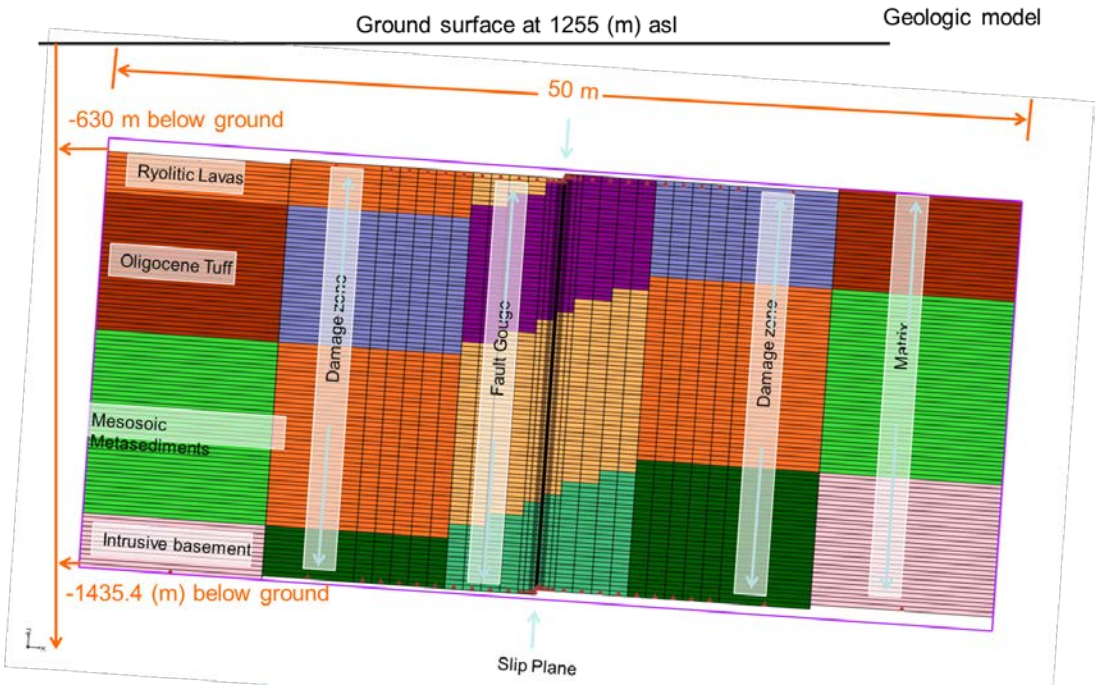

Figure 3-4. Conceptual model and grid for the Desert Peak 2D model. The 2D-fault has slip-plane (10^{-2} m in thickness), gouge (5 m on both side of slip plane), damage zone (10 m on both side of gouge) and intact matrix (10 m on both side of damage zone). The different rocks may change their hydrogeologic parameters if they are a part of the damage zone, gouge, and slip plane. Geology is after Faulds and Garside (2003). (a) no vertical or horizontal exaggeration; (b) 40 times horizontal exaggeration.

Although our conceptual model is simplistic, we consider it to be sufficient for showing some of the complexities that arise during injection of CO_2 into a normal fault and to reveal some of the challenges for geophysical imaging. Follow-up numerical experiments should consider 3D geometry and injection into conjugate faults such as those at Dixie Valley, Nevada.

Figure 3-5 shows the results of the example case of a homogeneous fault gouge. Because of the buoyancy and lower permeability in the basement rock, most of the CO_2 flows upward along the fault gouge against the hanging wall. The CO_2 does not enter the damage zone because of its lower permeability and higher capillary pressure at the brine–scCO_2 interface (Borgia et al., 2013). In less than 4 days of injection, the CO_2 reached the top of the computational domain. Because of decompression, the CO_2 plume tends to expand in the *x*-direction at its upper extent, creating a "tooth" in 2 days of injection (Figure 3-5b). After 4 days, the entire fault gouge was filled with about 4 m (thickness) CO_2 (Figure 3-5c). Most of these details of the flow are not evident in the model results shown without horizontal exaggeration (Figure 3-5e).

During the corresponding pull (production) process (not shown here for brevity) with production specified by setting pressure 0.4 MPa below hydrostatic pressure at the same depth where CO_2 was injected, practically no CO_2 is recovered back into the well. Instead water flows back into the fault gouge largely supplied by water along the footwall side of the gouge.

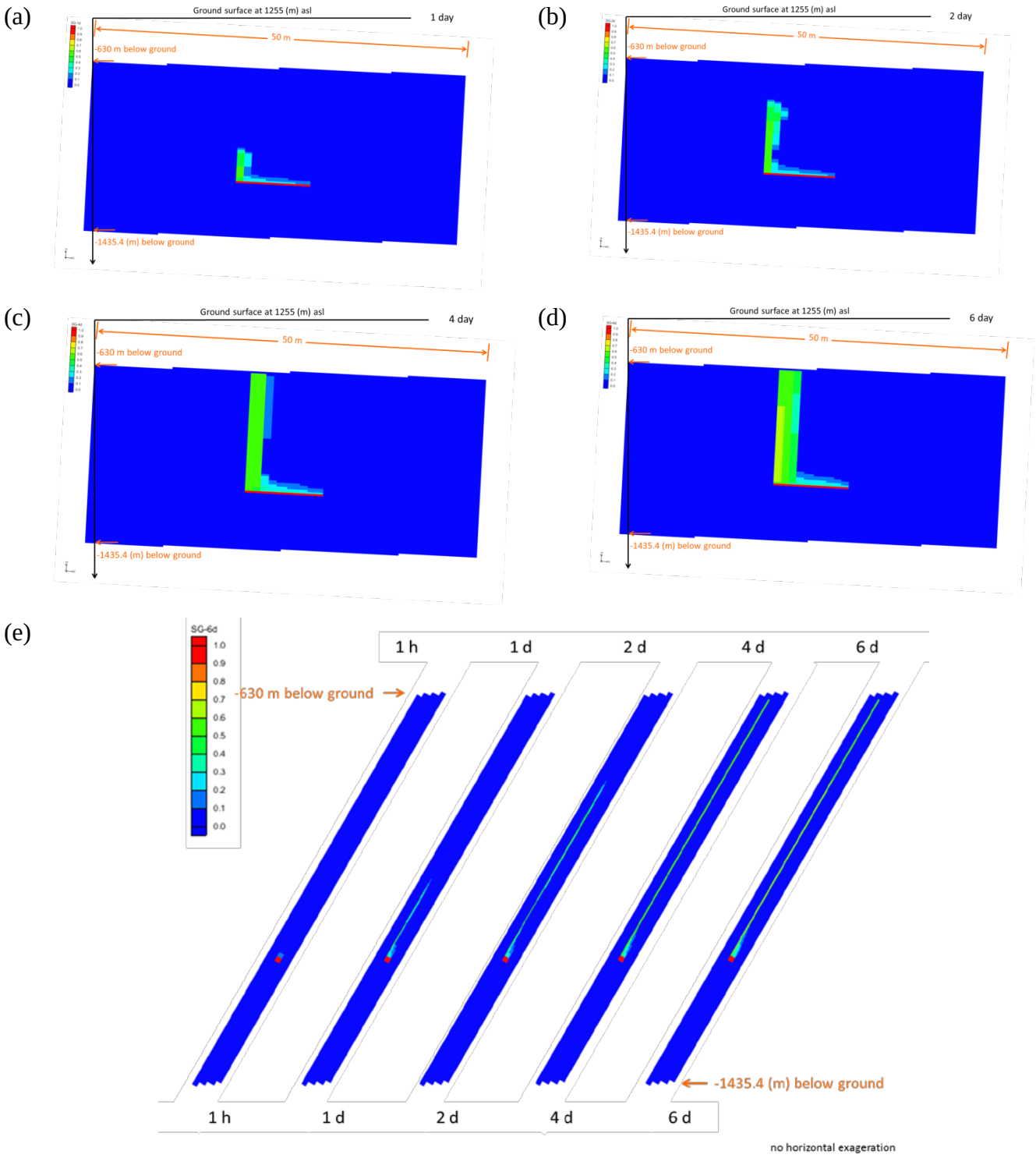

Figure 3-5. 2D model of CO_2 injection in a "Brady's-type" normal fault with 60° of dip. Fault gouge and slip plane are homogeneous in hydrogeologic properties. Note how the CO_2 plume develops against the hanging wall of the fault not entering the damage zone in the short time of the simulation. Note also the tooth that develops at the top of the plume. a) 1 day, b) 2 days, c) 4 days, d) 6 days, and e) the same results with no horizontal exaggeration. The inclined red line is made by the injection cells within the fault gouge.

4 WELL LOGGING

4.1 Introduction

Well logging provides a method of characterizing the fault zone following injection of CO_2 into the fault. Well logging could be conducted on a similar schedule as active seismic monitoring, i.e., before, during, and after the CO_2 push-pull test. Utilization of the well for logging will require accessing the injection well. The high-temperature of EGS sites (T > 175 ºC) limits the number of tools available for wireline well logging, and requires the use of so-called "hostile environment" (high-temperature) versions of the tools. In this section, we summarize our analysis of the potential for well logging to complement active seismic monitoring for characterizing faults and fractures during CO_2 push-pull.

4.2 Methods

We used simple methods to evaluate the likelihood of various existing high-temperature well-logging approaches to be effective in detecting time-lapse changes due to CO_2 injection. We used simple mixing models for fluid density, Gassmann model for effective elastic properties, and Archie's law for effective conductivity to estimate changes expected in effective properties across the various regions of a fault zone or fracture at geothermal reservoir conditions.

4.3 Results

The logging approaches we investigated are shown in Figure 4-1 along with indication of the feasibility of the measurements for detecting changes in the various properties over their possible ranges of saturation, salinity, pressure, and temperature in EGS systems. In our previous summary of this project (Oldenburg et al., 2016), we noted that there is only a limited set of logging tools available for the EGS environment due to the high pressure, high temperature (HPHT) conditions. As shown in Figure 4-1, the tools are expected to be sensitive to saturation, and to lesser degree, salinity. None of the tools is expected to be sensitive to ΔP or ΔT given expected ranges for these properties.

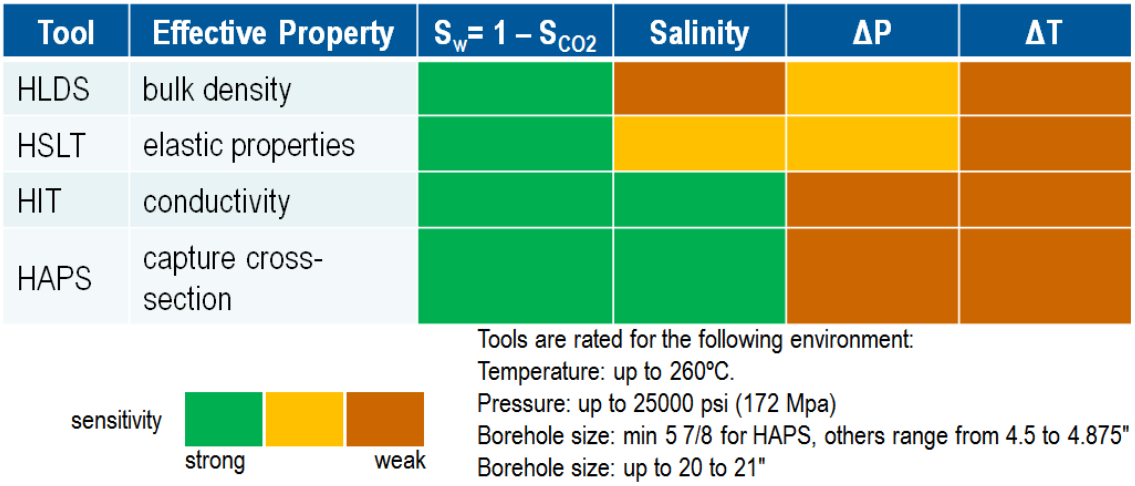

Figure 4-1. Wireline well-logging tools showing estimated sensitivity based on the computed dynamic range for effective properties (bulk density, elastic properties, conductivity, and neutron capture cross section) for expected ranges of $S_w = 1 - S_{CO2}$, salinity, *P*, and *T*. HLDS = Hostile Environment Litho-Density Sonde; HSLT = Hostile Sonic Logging Tool; HIT = Hostile environment Induction imaging Tool; HAPS = Hostile Accelerator Porosity Sonde.

In Figure 4-2, we present the results of estimated tool feasibility for the ranges of fluid properties expected in the CO_2 push-pull process investigated here in the various domains (matrix, damage zone, fault gouge, and slip plane). As discussed in Section 1.3.4, free-phase CO_2 tends not to enter the matrix, so no changes are expected in that domain. In contrast, the fault gouge receives most of the CO_2 so we expect changes in effective properties there, aided by a relatively high assigned porosity of 10 %. Specifically, effective conductivity and neutron capture cross section are expected to exhibit measurable changes in the gouge because the free-phase CO_2 displaces water, which may be saline thereby creating an even better signal.

It is notable that the well logging tool feasibility analysis found that bulk density and elastic properties were not expected to change enough in the CO_2 push-pull process to make the HLDS and HSLT tools useful in any of the regions (matrix, damage zone, fault gouge, or slip plane) (Figure 4-2). This would suggest that active seismic approaches, which rely on changes in elastic properties, might also not be feasible. But we note that the well-logging analyses considered here assume homogeneous rock around the well and that well logging only samples a small region around the well. Field-scale active seismic monitoring, on the other hand, interrogates a larger and more heterogeneous region of varying geometry that can enhance the contrast provided by injected CO_2.

Sensitivity calculations (not shown here) suggested that induction logging (electrical conductivity) would be the most promising measurement, although it would require either an open-hole environment or fiber-glass casing. Calculations also showed that neutron capture cross-section monitoring might be feasible for the fault gouge (and limited for slip-plane and damage zone), provided there is enough salinity contrast, a condition that could be achieved by carrying out a pre-flush with high-salinity brine. Neutron capture logging in HPHT environment can be performed using the Hostile Accelerator Porosity Sonde (HAPS) as part of

Schlumberger's Xtreme HPHT well logging platform. Neutron capture is sensitive to formation properties around 5-10 inches (13-25 cm) into the formation.

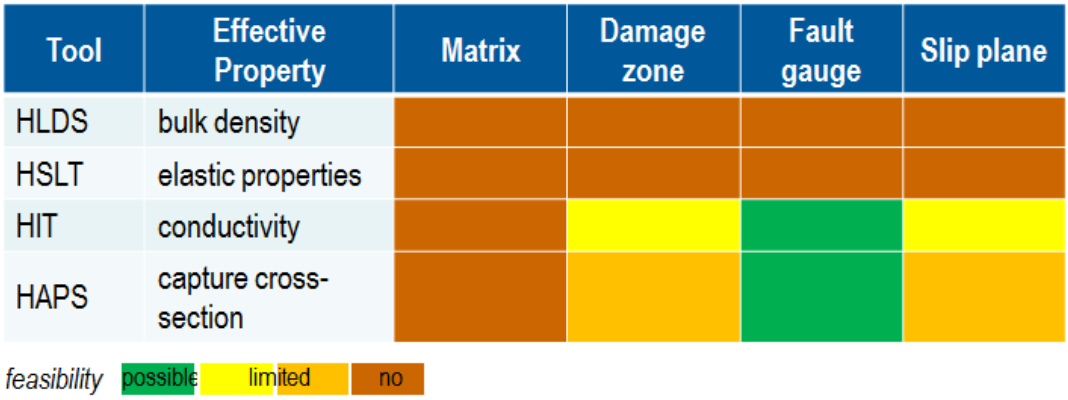

Figure 4-2. Wireline well-logging tools showing estimated feasibility for detecting effective property (bulk density, elastic properties, conductivity, and neutron capture cross section) changes in the various domains of the CO_2 push-pull system (matrix, damage zone, fault gouge, and slip plane). HLDS = Hostile Environment Litho-Density Sonde; HSLT = Hostile Sonic Logging Tool; HIT = Hostile environment Induction imaging Tool; HAPS = Hostile Accelerator Porosity Sonde.

4.4 Simulations of Neutron Capture

We present results of simulations based on a simplified effective medium model (Chugunov et al., 2013) derived using the software package SNUPAR (McKeon and Scott, 1989) for time-lapse neutron capture logging of the well at various potential locations intersecting the fault zone partially permeated by CO_2. Neutron capture cross-section measurements (Σ, expressed in capture units) use a high-energy neutron source generating pulses of about a billion 14 MeV neutrons per second and γ-ray detectors. The tool detects a γ-ray response that directly corresponds to the absorption (capture) of a thermal neutron by nuclei of fluids and rock matrix surrounding the tool. In HPHT environment, time-lapse differences in Σ greater than 1 capture unit are needed for positive detection of CO_2. The measured signal contains contributions from the matrix and the fluid making it a function of porosity, salinity, saturation, pressure, and temperature. These properties are simulated using TOUGH2-ECO2N as presented in Section 1.3, and passed to the SNUPAR code for simulating the nuclear logging tool response. Under simplifying assumptions, rock matrix contributions cancel out in the time-lapse mode, while the remaining fluid contribution is sensitive to CO_2 saturation and decreases approximately linearly with the displaced brine saturation. The SNUPAR-based simulation results are presented in Figure 4-3 after six days of injection. Results of $\Delta\Sigma$ response are computed along seven profile lines shown in Figure 4-3 by the various colored symbols corresponding to different distances from the slip plane where X = 25 m is the slip plane. Neutron capture measurement appears to be an effective tool to supplement active seismic monitoring to locate CO_2 in the fault zone.

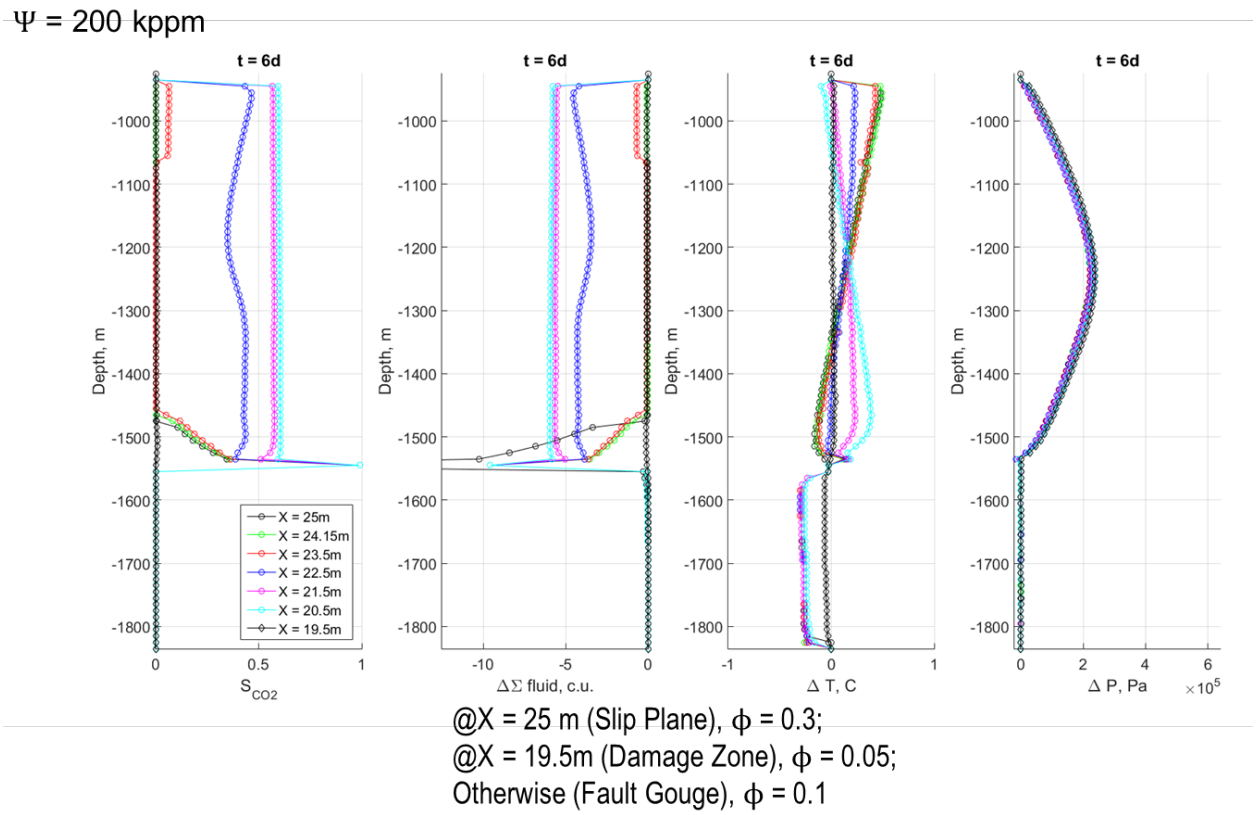

Figure 4-3. Profiles of simulation results at 6 days from the SNUPAR code using the output of the TOUGH2-ECO2N runs as input. Colored symbols correspond to different sub-vertical profile lines through the system starting at the slip plane (X = 25 m) and moving to the left to X = 19.5 m. The second frame from the left shows a strong time-lapse capture cross-section signal that suggests that CO_2 can be monitored using neutron capture logging in the considered EGS setting.

4.5 Conclusions

Availability of well-logging tools is limited in the EGS environment due to high temperature (T > 175 °C). In general, multiple fractures and wide fault zones will favor imaging by both active seismic and well-logging approaches. Dynamic range calculations and simple analyses suggest that induction logging (electrical conductivity) and neutron capture monitoring might be feasible for tracking injected CO_2 in fault gouge, given a proper placement of the monitoring well. We note that the analyses here are simplified and involve only a small region around the borehole. The next step in the workflow to test the use of CO_2 injection for enhancing characterization of faults or fracture zones is to simulate the seismic response of the system as described in the next section.

5 MODELING OF ACTIVE SEISMIC MONITORING

5.1 Introduction

In this effort we simulate active seismic monitoring to address the question of whether CO_2 injected into faults and fractures can enhance detectability by active seismic approaches, and if so, can active seismic methods be used to characterize the fault or fracture zone? At the heart of this question is whether the CO_2 injection causes enough contrast in elastic properties over enough volume to affect seismic wave propagation at a level that is resolvable by the measurements.

5.2 Methods

Fundamentals

Our approach is to simulate active-source seismic monitoring using finite-difference (FD) solutions to wave propagation equations as implemented in a code originally from SPICE (http://www.spice-rtn.org/library/software.1.html), which has been modified at LBNL for parallel processing, different boundary conditions, and for consideration of fracture properties. Forward modeling of faults and fractures typically uses equivalent media approximations. We use two approaches to velocity changes due to fluid injections in fractures: 1) velocity change due to changing fluid saturation in fractures can be treated as occurring in an equivalent isotropic porous media (with modified velocity in the fracture region); 2) velocity change in a discrete fractured region treated as changes in fracture compliance in an anisotropic media..

Our FD approach uses an explicit gridded finite-difference technique introduced by Madariaga (1976), Virieux and Madariaga (1982), and Virieux (1986). A perfectly matched layer (PML) boundary condition is used to reduce undesirable edge effects (Roden and Gedney, 2000; Komatitsch and Martin, 2007; Martin et al., 2008a; b; Martin and Komatitsch, 2009). For 3D calculations, an MPI (Snir et al., 1998) approach is implemented to improve computational efficiency. Our approach to the inclusion of fractures follows the method of Coates and Schoenberg (1995) using a fracture compliance approach to anisotropic finite-difference modeling. The change in fracture compliance caused by CO_2 displacing brine in fractures is calculated using the method of Nakagawa and Schoenberg (2007), while CO_2 displacing brine in equivalent porous media uses Gassmann fluid substitution.

We model an active source which will send out seismic waves through the target zone to be reflected by the interfaces of rock volumes with different velocities or by discrete discontinuities such as fractures. By assessing properties of the modeled reflected waves on the free surface or within specific seismic monitoring boreholes, we can infer effective rock properties as would be done in a field experiment.

Seismic wave propagation is modeled by using a constitutive linear-elasticity equation, which can be derived from a generalized Hooke's law. By this approach, the 3D anisotropic stress-strain relationship is linearized through stiffness and/or compliance tensors (e.g. Nemat-Nasser and Hori, 1999). Eq. 1 shows the stress ($\boldsymbol{\sigma}$) and strain ($\boldsymbol{\varepsilon}$) relationships in term of stiffness tensor ($\boldsymbol{C}$) and compliance tensor ($\boldsymbol{S}$), which also shows the inverse relationship between $\boldsymbol{C}$ and $\boldsymbol{S}$.

$$\begin{aligned} \sigma &= C \cdot \epsilon \\ \epsilon &= S \cdot \sigma \\ C &= S^{-1} \end{aligned} \tag{1}$$

Note also the reversal of symbol name relative to first letter of the words “stiffness” and “compliance.” Thus, the 3D anisotropic stress-strain relationship for seismic wave propagation can be written in compressed notation, for transversely isotropic media (Virieux, 1986; Etgen, 1987; Daley et al., 2006), as shown in Eq. 2. Note that C_{11} relates fracture normal stress and strain, as utilized in following sections.

$$\begin{bmatrix} \sigma_{xx} \\ \sigma_{yy} \\ \sigma_{zz} \\ \sigma_{yz} \\ \sigma_{xz} \\ \sigma_{xy} \end{bmatrix} = \begin{bmatrix} C_{11} & C_{12} & C_{13} & 0 & 0 & 0 \\ C_{21} & C_{22} & C_{23} & 0 & 0 & 0 \\ C_{31} & C_{32} & C_{33} & 0 & 0 & 0 \\ 0 & 0 & 0 & C_{44} & 0 & 0 \\ 0 & 0 & 0 & 0 & C_{55} & 0 \\ 0 & 0 & 0 & 0 & 0 & C_{66} \end{bmatrix} \times \begin{bmatrix} \epsilon_{xx} \\ \epsilon_{yy} \\ \epsilon_{zz} \\ 2\epsilon_{yz} \\ 2\epsilon_{xz} \\ 2\epsilon_{xy} \end{bmatrix} \tag{2}$$

Fluid and Rock Properties

In order to model seismic wave propagation in isotropic porous media, estimates of the bulk fluid- and rock-mixture properties are needed. We use the bulk modulus of the dry rock (K_d), bulk modulus of the mineral matrix (K_s), bulk modulus of the fluid (K_f), porosity (ϕ) to calculate the bulk modulus of the fluid-filled rock (K_b) using the Gassmann equation

$$K_b = K_d + \frac{\left(1 - \frac{K_d}{K_S}\right)^2}{\frac{\phi}{K_f} + \frac{1-\phi}{K_f} - \frac{K_d}{K_S^{\,2}}} \tag{3}$$

The isotropic p-wave velocity is a function of K_b, dry shear modulus (μ_d), and bulk density (ρ_b):

$$V_p = \sqrt{\frac{K_b}{\rho_b} + \frac{4}{3}\frac{\mu_d}{\rho_b}} \tag{4}$$

We use an accurate equation of state model to estimate CO_2 and water properties to calculate K_f, and representative values of K_S and K_d for various rock types (Altundas et al., 2013). The workflow for estimating V_p is shown in Figure 5-1. We assumed homogeneous fluid mixing (the typical Gassmann relation) rather than a more complex patchy saturation model.

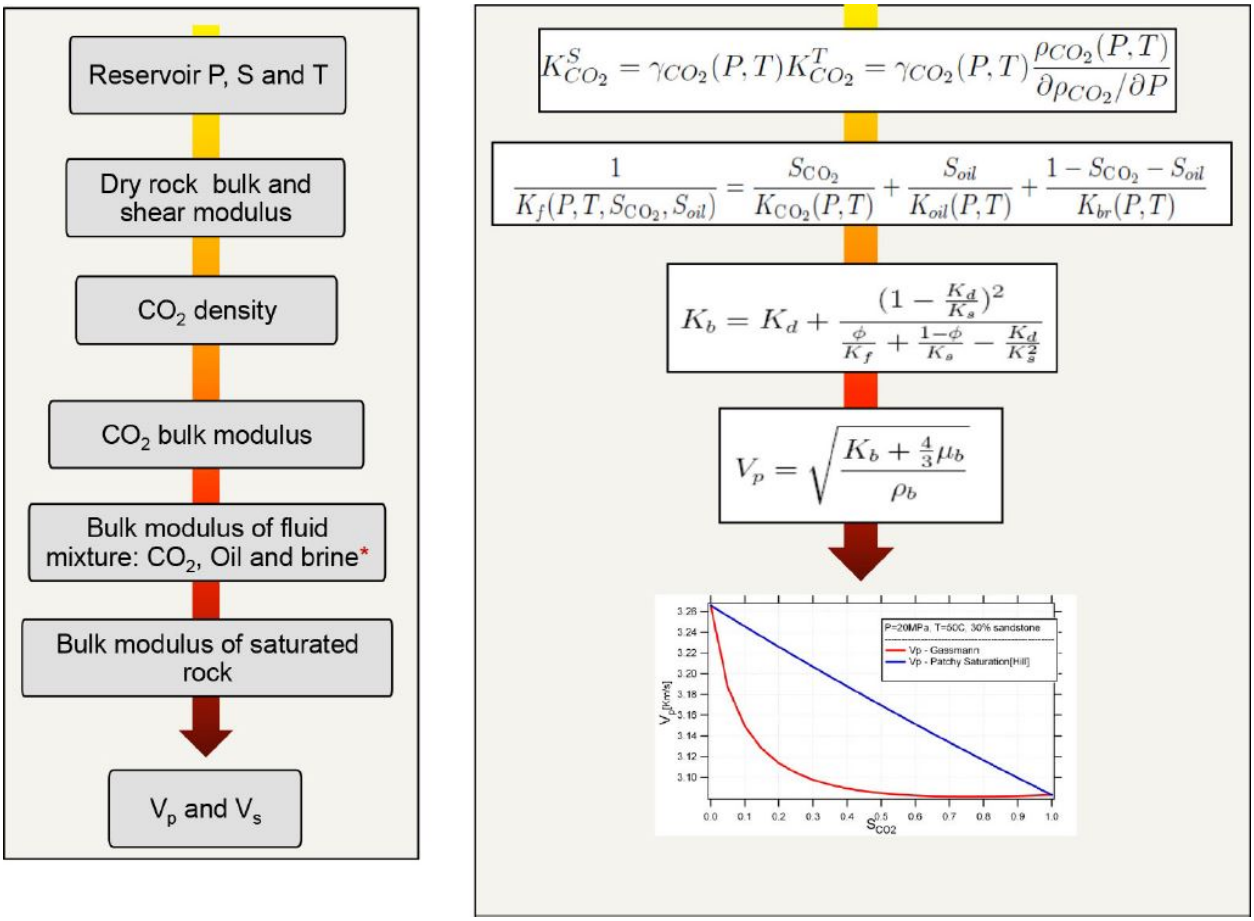

Figure 5-1. Workflow for modeling V_p and V_s as functions of dry and bulk rock properties and fluid properties.

5.3 Results

Model System

The prototypical Brady's conceptual model used for simulating the CO_2 push-pull (Figure 5-2) is augmented with seismic velocities as shown in Figure 5-2 for modeling active seismic monitoring. Because the injected CO_2 largely stays within the fault zone, we model the region around the fault in detail as shown in Figure 5-3. Note the large horizontal exaggeration of Figure 5-3.

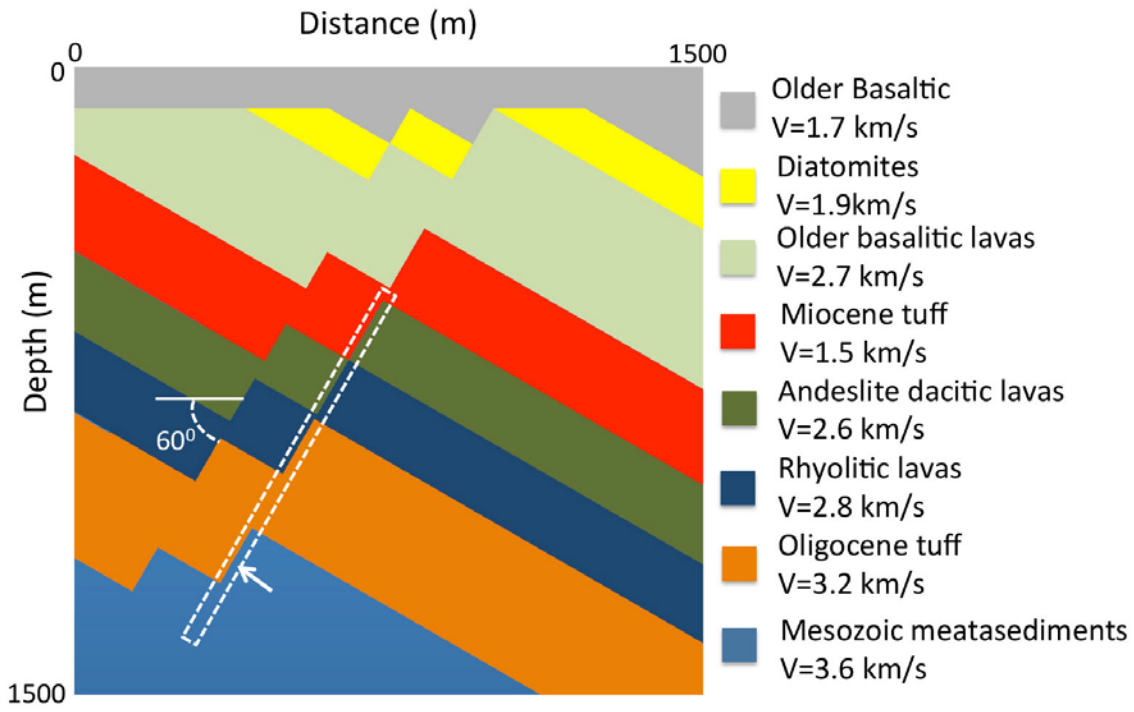

Figure 5-2. P-wave velocity model of the conceptual Desert Peak geothermal field. Schematic cross-section of the Rhyolite Ridge fault zone after Faulds et al. (2010b). Only the right-most (ESE) fault is used in the hydrogeologic modeling (white dashed box).

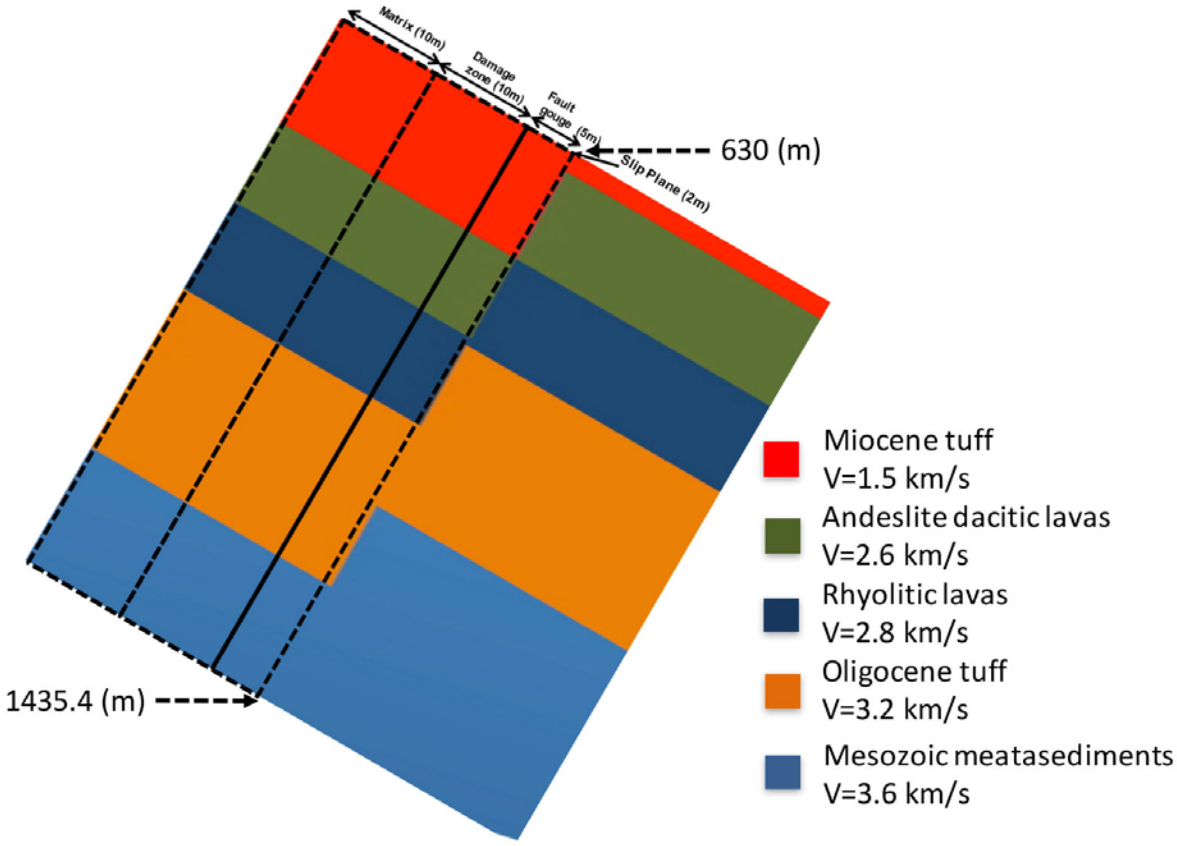

Figure 5-3. The fault zone within the white dashed rectangle in Figure 5-2 is elaborated with 20 times width-along-strata exaggeration. The widths of the matrix, the damage zone, the fault gouge, and the slip plane are 10 m, 10 m, 5 m, and 2 cm, respectively, and the vertical depth of the field ranges from 630 to 1435.4 m below ground (cf. Borgia et al., 2017b)

Changes in Stiffness

Preliminary to presentation of active seismic results, and to connect the seismic modeling with the theory presented above, we present in Figure 5-4 the calculated changes in the C_{11} (normal component of stiffness from Equation (2) above) resulting from the changes in saturations simulated by TOUGH2/ECO2N as presented in Section 1.3. As shown in Figure. 1.5-3, changes in CO_2 saturation changes the elastic moduli (e.g. the stiffness component, C_{11}) in a very narrow region of the fault gouge and slip plane. The active seismic monitoring planned for enhancing the characterization of such a fault will need to resolve changes in seismic velocity at the scale of the CO_2-filled gouge region of the fault zone. In the following, we treat this thin region as an equivalent porous media with velocity changes calculated using the Gassmann approach.

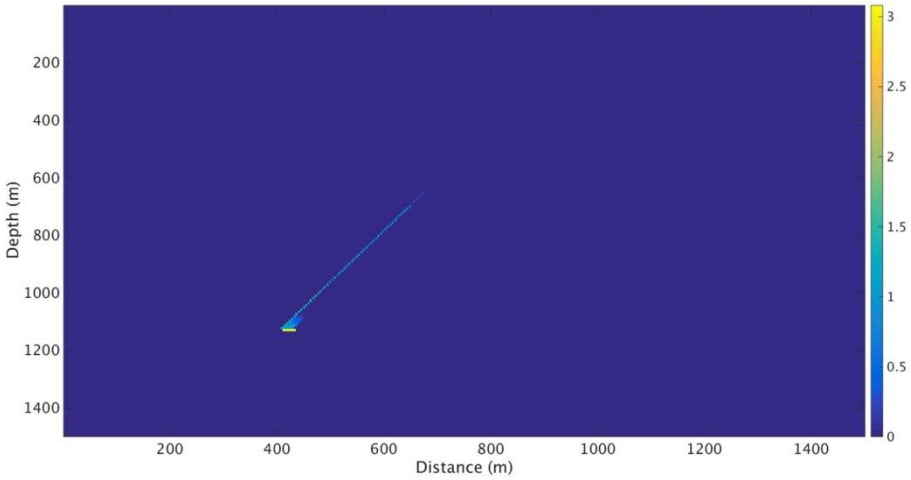

Figure 5-4. Changes in C_{11} (GPa) arising from CO_2 saturation in the fault zone as simulated in the push phase shown in Figure 3-5.

Changes in Vp

Over the course of the project, we simulated time-lapse seismic in surface, VSP, and crosswell seismic configurations. For brevity in this summary report, we present here only the crosswell configuration results, which are the most promising for detecting and characterizing fault-zone CO_2. Other results are available in a manuscript currently in preparation.

The crosswell seismic survey is carried out with sources and receivers straddling the fault, deep below the overburden and weathering zones, which usually cause strong attenuation and dispersion effects on seismic waves. Crosswell seismic typically gains resolution from use of higher frequency data. Therefore, the crosswell survey is capable of resolving small features that are more difficult to image with surface and VSP seismic. We note that crosswell surveys have been used successfully for monitoring CO_2 injection operation within GCS projects (Wong et al., 1987; Harris et al., 1995; Schaack et al., 1995; Rector et al., 1995; Lazaratos et al., 1995; NolenHoeksema et al., 1995; Daley, et al., 2008).

A profile of the velocity model we use is shown in Figure 5-5. As shown, there is an overall decrease in p-wave velocity in the layered volcanics of the system. Superimposed on this variation is the CO_2-induced change in p-wave velocity as calculated using the methods described in Section 1.5.2. The time-evolution of the CO_2 saturation simulated with TOUGH2/ECO2N (see Section 1.3) provides the basis for p-wave changes as CO_2 is injected.

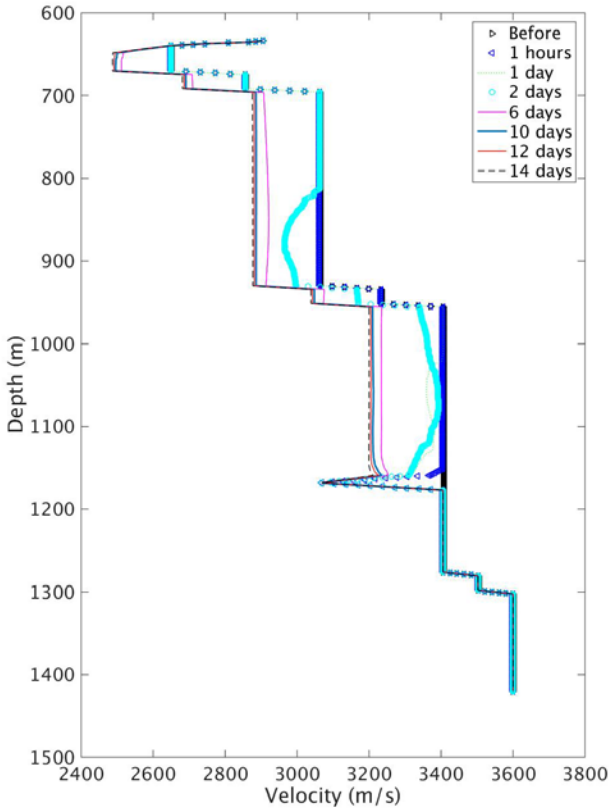

Figure 5-5. 1D velocity models 3 m from the slip plane into the hanging wall fault gouge.

Figure 5-6a shows the schematic of the crosswell survey with the two wells 150 m apart. The sources are placed in the well on the left-hand side at a depth from 1100 to 1250 m with 1 m spacing; the same depth and spacing configurations are used for the receivers in the well on the right-hand side. Figure 5-6b shows the corresponding synthetic seismograms pre- and post CO_2 injection. Cursory inspection of the seismograms corresponding to pre- and post CO_2 injection suggests that little change occurs after two days of CO_2 injection. But looking at the time-lapse difference of the same seismograms, we observe about 10% amplitude difference, which may be a measurable quantity. Considerations for extending these modeling results to field demonstration are discussed in Section 1.7.

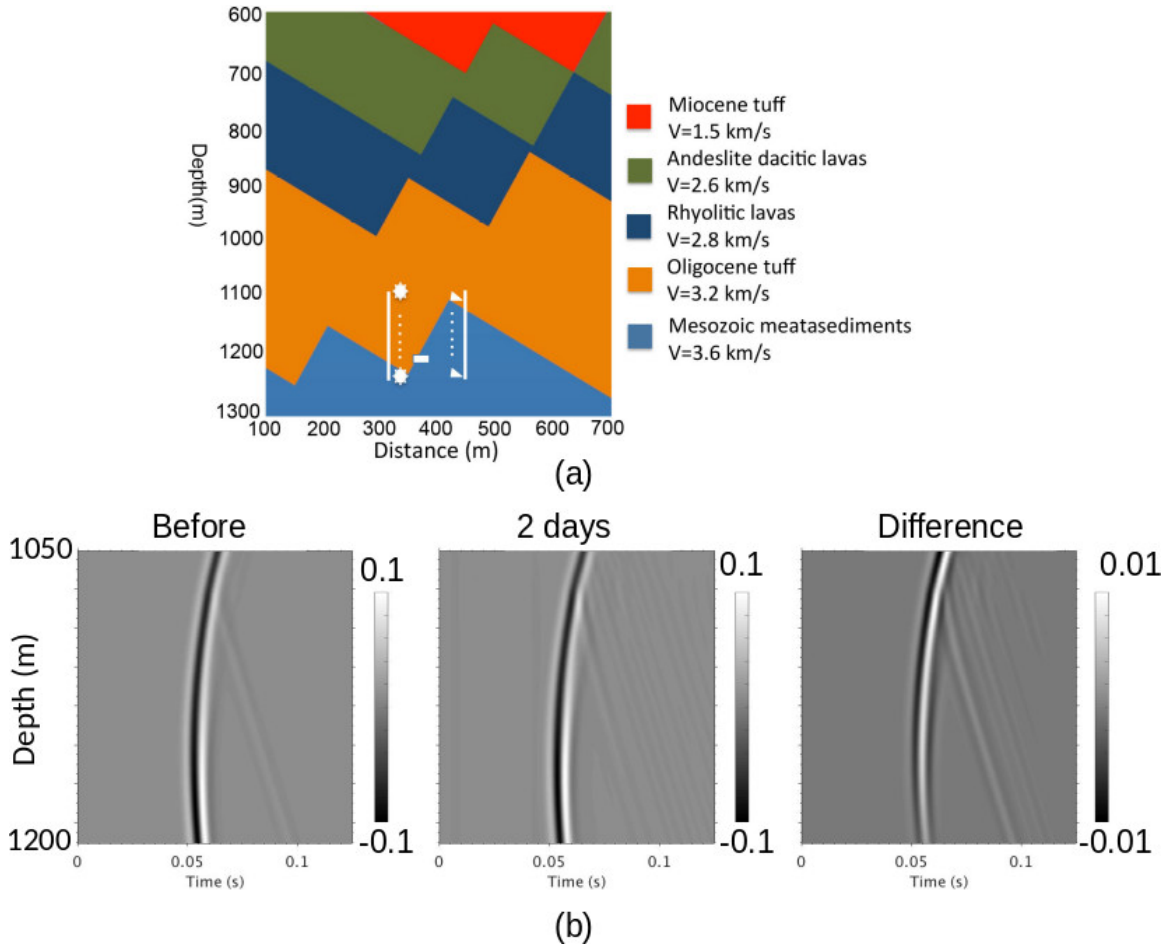

Figure 5-6. (a) shows crosswell survey geometry with the P-wave velocity model; (b) shows the modeled seismogram.

Detection of change in seismic data is one goal, however the correct spatial localization of change is a separate goal which requires seismic "imaging." Imaging is a numerical data processing activity that places seismic energy, recorded using an arbitrary geometry with an arbitrary velocity model, in its correct subsurface location. A modern imaging method is known as reverse time migration (RTM) (e.g., Baysal et al., 1983). To enhance the characterization of the fault zone via seismic imaging, we carried out reverse time migration of the synthetic crosswell monitoring data using the method of Zhu, et al. 2014. Figure 5-7a shows the seismic velocity model corresponding to CO_2 saturations, *P*, and *T* from the TOUGH2/ECO2N simulations and source and receiver configuration in crosswell setting around the fault. An example of seismograms from one source at one time (forming a wavefield "snapshot") is shown in Figure 5-7b. Figure 5-8a shows the seismograms corresponding to pre- and post CO_2 injection, and their difference (bottom). Corresponding RTM images and their difference (bottom right-hand image) can be seen in Figure 5-8b. As shown, the difference RTM shows a dipping structure that represents the fault where CO_2 saturation appears to be high. This result demonstrates the possibility that CO_2 injection along with active seismic imaging can be used to locate and orient faults into which CO_2 is injected. Comments on the reliability and robustness of this result are presented in the Discussion section.

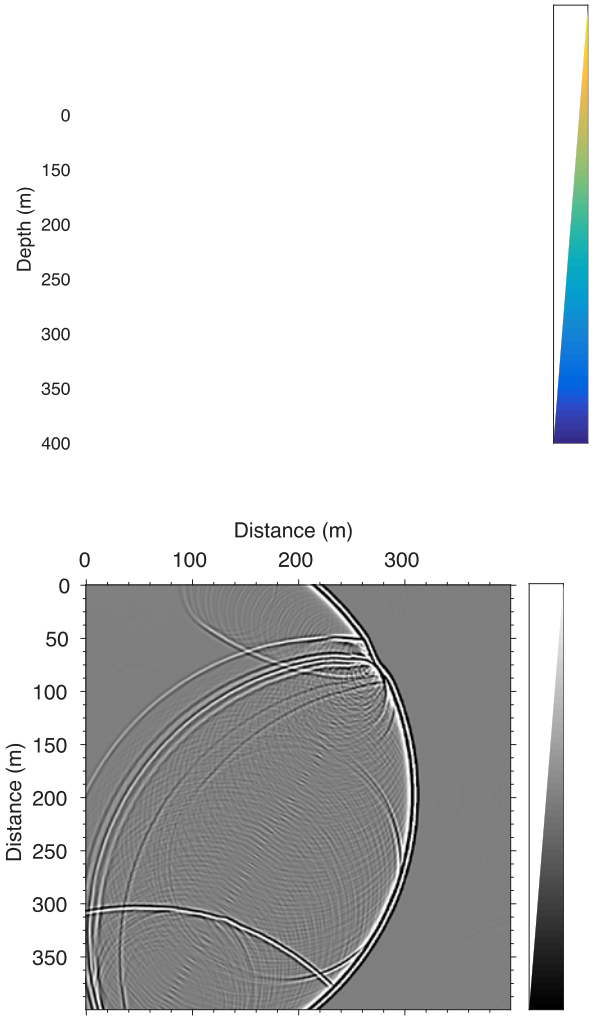

Figure 5-7. (a) Crosswell survey geometry with the P-wave velocity model with CO_2 in the gouge of the fault zone; (b) Modeled wavefield from one source at one time (a wavefield snapshot) with labeled reflection events.

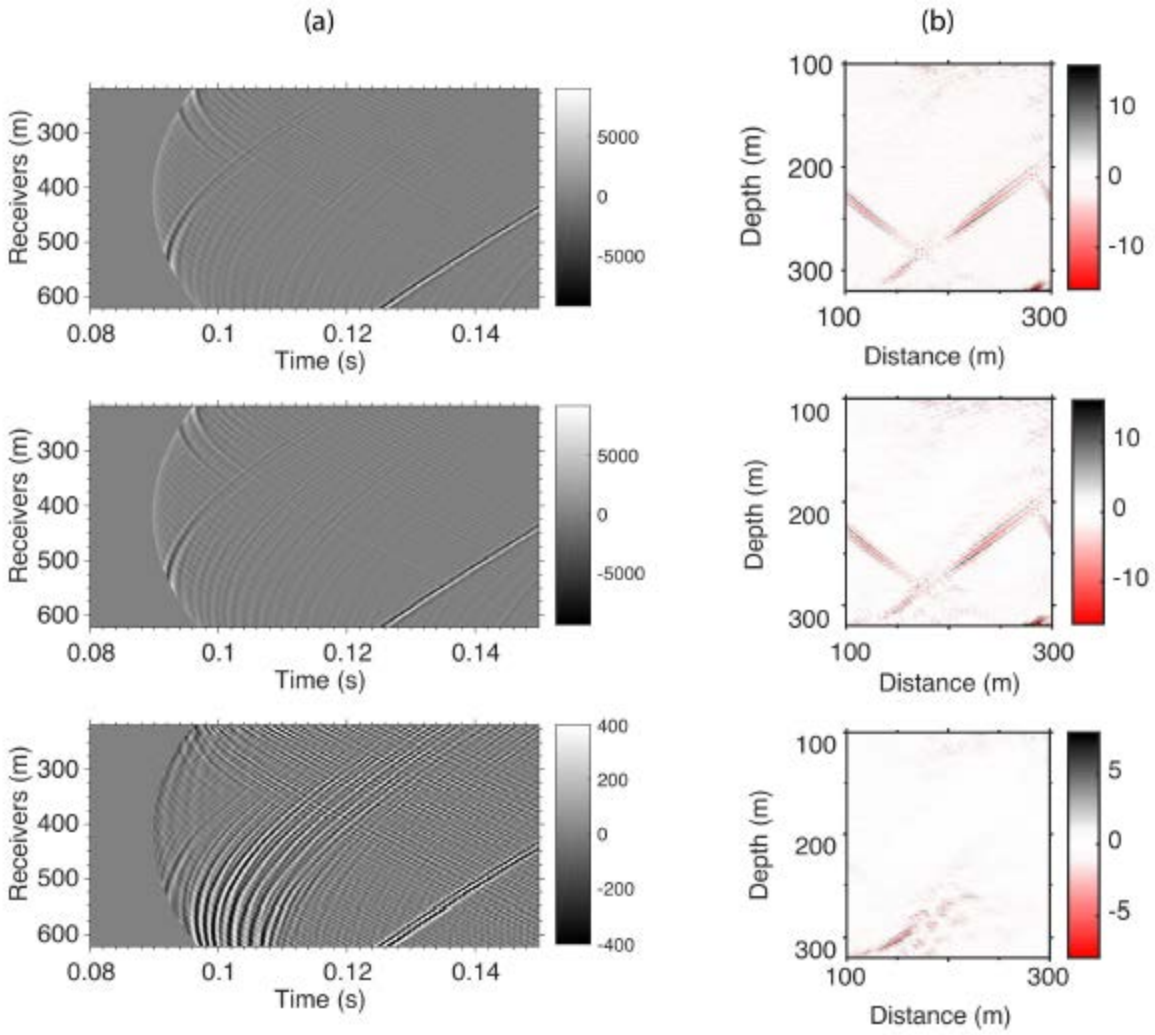

Figure 5-8. (a) Seismograms of pre- (top) and post- (middle) CO_2 injection after two days and the difference (bottom). (b) Results of reverse-time migration of pre- and post-CO_2 injection seismograms and their difference (bottom).

5.4 Conclusions

We have modeled the effects of CO_2 injection into a fault at a prototypical EGS site. The result of CO_2 saturation in the fault zone is modeled as a decrease in the p-wave velocity across the fault. Finite-difference modeling of active-source seismic in a crosswell geometry suggests that the injected CO_2 can be imaged. The simulation results show that VSP and crosswell surveys are able to capture the CO_2 plume more effectively. Both methods are conducted in boreholes, giving improved geometry, and furthermore we expect borehole methods to experience much less near-surface attenuation (although this was not explicitly modeled). Once the CO_2 plume is detected, reverse-time migration can be used to correctly image the fault zone containing the CO_2. The magnitude of the changes in seismic amplitude created by CO_2 injection is approximately 10%, which is not large but is within the range relevant to field deployments that

acquire very high-quality data, e.g., through design of acquisition geometry that enhances signal to noise ratio. Additional details will be presented in Zhang et al. (in prep.).

6 PRESSURE TRANSIENT AND SENSITIVITY FOR SINGLE FAULT

6.1 Introduction

In this study, we evaluated the feasibility of using pressure transient monitoring during CO_2 push-pull tests to complement active seismic and wireline well logging for EGS characterization. For this purpose, we used a 2D model of the prototypical geothermal site (Desert Peak, NV) with a single fault. Through numerical simulation using iTOUGH2, we found that the pressure transient at the monitoring wells in the fault gouge shows unique traits due to the multiphase flow conditions developed by CO_2 injection, and varies sensitively on the arrival of the CO_2 plume and the degree of CO_2 saturation. A sensitivity analysis shows the pressure transient is most sensitive to the fault gouge permeability, but also depends on multiphase flow parameters and the boundary conditions of the fault. Some highlights of the study are summarized in this section, with details available in the full manuscript that is currently in review (Jung et al., 2018).

6.2 Methods and Model System

We used TOUGH2/ECO2N V2.0 (Pruess et al., 2012; Pan et al., 2014) to develop a model and simulate the two-phase flow of CO_2 and water during CO_2 push-pull injection-production. This code is able to simulate two-phase flow in the pressure and temperature range up to 600 bars and 300 °C, respectively, and is therefore appropriate for EGS applications. Here, consistent with the terminology in TOUGH2/ECO2N, a CO_2-rich non-wetting phase is referred to as a gas phase. iTOUGH2-PEST (Finsterle, 1993; Finsterle, 2004; Finsterle et al., 2016; Finsterle and Zhang, 2011) is used for sensitivity and inverse analysis.

We adapted and expanded the 2D model domain originally developed by Borgia et al. (2017a; b) representing features of the Desert Peak geothermal field to explore the technical feasibility of CO_2 push-pull testing for EGS fault/fracture characterization for pressure transient analysis. The fault gouge, damage zone, and country rock matrix have distinct fluid-flow properties (i.e., permeability and porosity) along with typical multiphase flow properties (see Jung et al. (2018) for details). In our 2D model, the fault gouge is 5 m thick on both sides of the slip plane (10 m total), and the damage zone is 10 m thick on both sides of the fault gouge. The matrix is 200 m thick on both sides of the damage zone, which is sufficiently wide to minimize the effect of the side boundaries. The model takes into account the variable country rocks for the matrix, as color-coded in Figure 6-1.

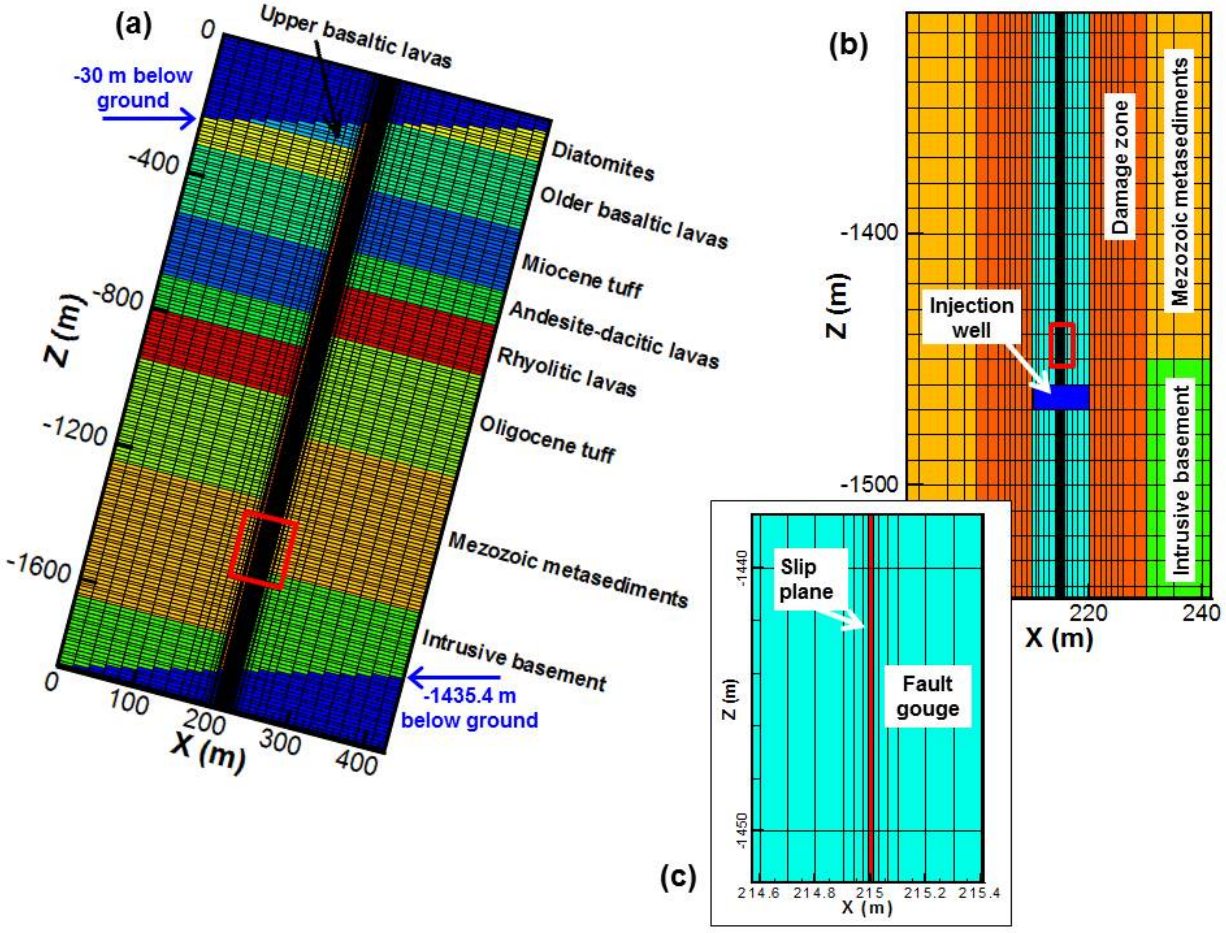

Figure 6-1. 2D model grid: (a) the whole model domain (note that the dark blue triangular areas at the upper left and lower right corner are not part of the actual model domain); (b) the local area around the well; (c) a close-up of the area near the slip plane, showing the fine discretization.

The initial hydrostatic condition (water table at 30 m depth) is used to calculate the pressure difference $\Delta P = P - P_{init}$, which is the variable used in this study to describe all pressure-related data (salinity is ignored). Temperature varies from 25 °C at the top boundary to 170 °C at the depth of 630 m with a geothermal gradient of 0.24 °C/m, and to 210 °C at the bottom boundary with the geothermal gradient of 0.05 °C/m, which approximately represents field observations. The top and bottom boundaries are open to flow and the side boundaries are closed.

The injection/production well is assumed to be open only in the fault gouge and slip plane, and a constant pressure of 0.3 MPa above and below the ambient hydrostatic pressure (ΔP_{inj} = 0.3 MPa and ΔP_{prod} = -0.3 MPa) is applied for injection and production of CO_2, respectively. CO_2 is injected for 4 days, then fluid comprising a mixture of CO_2 and brine is produced for 4 days from the same well. We assume that additional observation wells are available for pressure monitoring and frequent well logging for the purpose of fault characterization, and several potential locations along the fault gouge are considered. We assume that CO_2 saturation data are available as the result of neutron capture well logging analysis. Anticipating buoyancy effects on the CO_2 flow, the monitoring wells (MW) are located near the left-hand edge of the fault gouge (i.e.,

along the hanging wall) and are assumed to be located at 50 m, 100 m, and 200 m above the injection well along the *z*-direction (MW_{50m}, MW_{100m}, and MW_{200m}).

Figure 6-2 shows CO_2 and water flow from the injection well to the fault zone during the push and pull periods. Each curve in this plot represents the sum of the flows between the injection well and the adjacent fault zone grid blocks. A negative value means the fluid flows from the fault zone into the well. As the injection starts, the overpressure in the injection well forces both CO_2 and water to flow out of the well. The CO_2 flow gradually decreases as the pressure difference between the injection well and the surrounding fault zone decreases. The flow rate drops at 10^3 s as a CO_2 phase develops in the grid block right above the injection well, and slightly declines again at 2×10^4 s as the pressure pulse reaches the top boundary of the model (a constant-head water table). Unlike CO_2, which mostly flows upward during the push period, water flows downward except at very early times (~ 30 s). On the other hand, during the pull period, the underpressure relative to the initial hydrostatic pressure pulls both CO_2 and water back into the well in proportions equal to the local mobility. However, CO_2 is no longer produced after about 1.3×10^3 s due to buoyancy effects which carry CO_2 upward and out of the capture zone of the producing well. Water flow is reversed at late times, indicating the pressure above the production well is temporarily lower than that at the production well, a phenomenon discussed below.

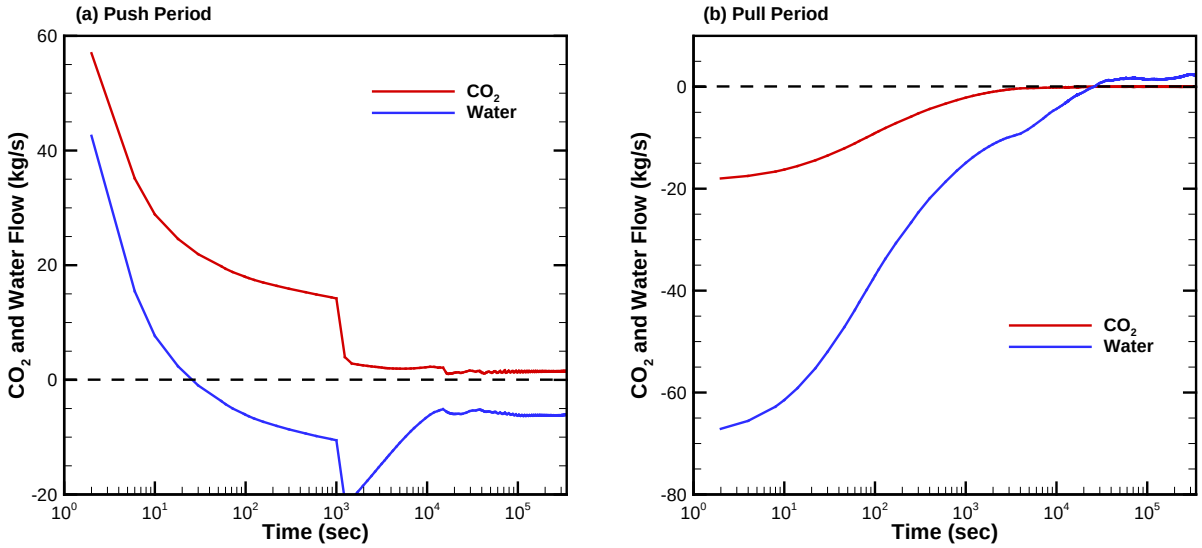

Figure 6-2. CO_2 and water flow during the (a) push and (b) pull period.

Figure 6-3 shows the spatial distribution of pressure difference (ΔP) and gas saturation during the push and pull periods. During the injection, the pressure pulse quickly propagates through the fault gouge and damage zone, taking only 2×10^4 s for the pressure pulse to reach the top model boundary through the fault gouge. The pressure also propagates relatively fast laterally through the andesite-dacitic lavas (see the distribution at the end of the push period at ~700 m depth), where the permeability is five times greater than that in the other country rock formations. As the fluid production starts after 4 days of CO_2 injection, underpressure relative to the initial hydrostatic pressure (i.e., negative ΔP) develops near the well, with the pressure decline most significant in the fault gouge during the pull period.

One thing that should be noted is that the maximum ΔP observed during the push period (~ 0.85 MPa) is higher than ΔP_{inj} (0.3 MPa), which is most evident at t = 4 day in Figure 6-3. This is due to the effect of a gas column being created in the gouge and the much smaller density of gas compared to water. Thus, the pressure at the top of the gas plume is similar to the (high) pressure at the base. As a result, the gouge water pressure becomes elevated thereby increasing the ΔP_{prod}.

During the push period, the injected CO_2 mainly flows upward through the fault gouge, specifically against the hanging wall due to buoyancy of CO_2. This is because the transmissivity of the gouge is more than two orders of magnitude greater than that of any other material. Only a limited amount of CO_2 enters the damage zone because of its lower permeability and higher capillary pressure at the water-CO_2 interface. During the pull period, the CO_2 plume keeps moving upward, driven by a strong buoyancy force, despite the underpressure at the well. As a result, the leading edge of the CO_2 plume has traveled about 1000 m upward in the z-direction by the end of the simulation time (after four days of injection and four days of production). This explains the low CO_2 recovery rate during the pull period. Due to decompression and local pressure increase, the CO_2 plume tends to expand in the x-direction as CO_2 flows upward; it is most prominent at the end of the pull period.

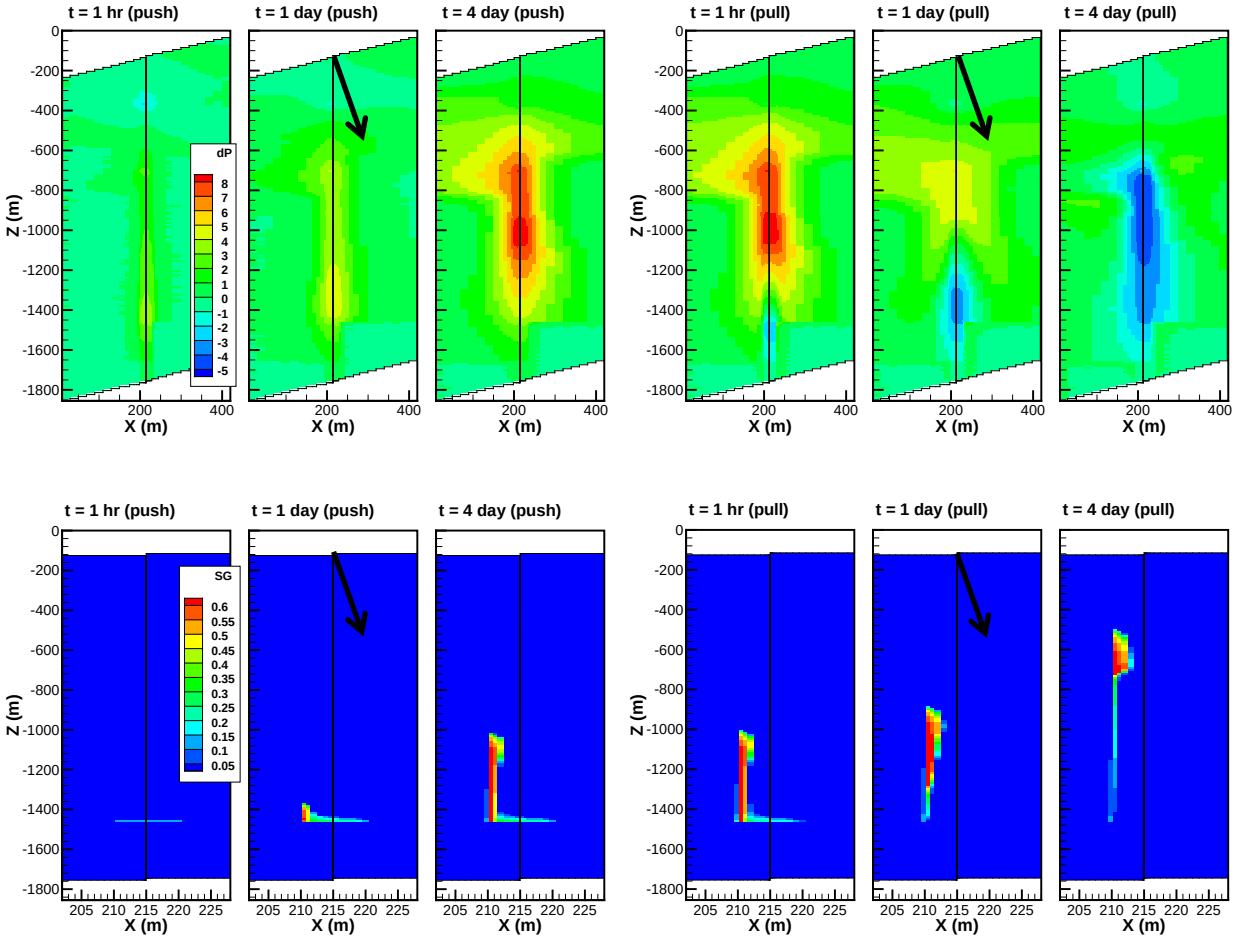

Figure 6-3. Spatial distribution of pressure change in bar (upper row) and gas saturation (lower row) at 1 hr, 1 day, and 4 days of the push and pull periods. Note that the actual grid is rotated clockwise by 30° to make the fault dip 60°; black arrows point in the vertical direction.

Figure 6-4 shows the temporal variation of pressure transient and gas saturation at the selected monitoring wells. The pressure transients at the monitoring wells MW_{50m}, MW_{100m}, and MW_{200m} in general show a similar pattern during the push period. As the CO_2 injection starts, the pressure propagates from the injection well and a gradual pressure increase is observed. The pressure increases rather steeply when CO_2 reaches the monitoring location due to decreasing total kinematic mobility, and drops when the CO_2 saturation reaches approximately 0.6, at which point the total kinematic mobility rises again according to the chosen relative permeability. Due to the distance from the injection well, the pressure transient increases in consecutive order from MW_{50m} to MW_{200m}. In addition, the injected CO_2 decompresses as it rises upward through the hydrostatic pressure of the resident water.

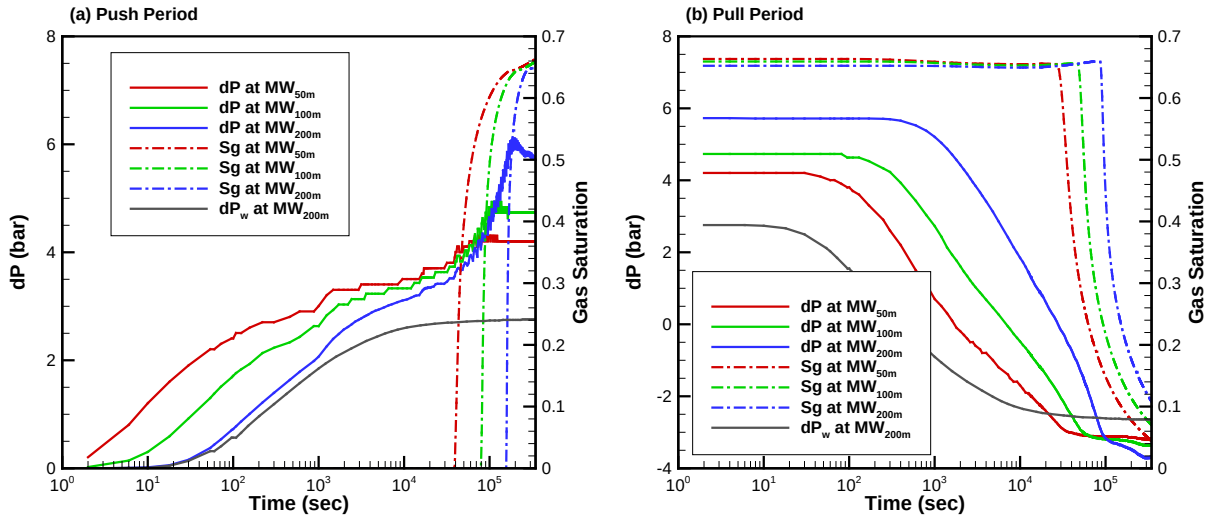

Figure 6-4. Pressure transient (solid) and gas saturation (dash-dot) at MW_{50m}, MW_{100m}, and MW_{200m} during the push and pull periods. As a reference case, a pressure transient with water as an agent for the push-pull test (ΔP_w at MW_{200m}) is also shown.

The oscillations observed in the pressure transient during the push period are due to spatial discretization error. When CO_2 phase enters a grid block (e.g., CO_2 enters the grid block right above the injection well at ~10^3 sec), the grid block undergoes a transition from a single aqueous phase to a two-phase mixture. The liquid relative permeability drops rapidly while the gas relative permeability increases rather slowly, resulting in a reduction of the total kinematic mobility of the fluid. As the gas saturation increases, the increase in gas relative permeability becomes greater than the decrease in liquid relative permeability. This pattern repeats every time CO_2 enters a new grid block.

During the pull period, the pressure transients at MW_{50m}, MW_{100m}, and MW_{200m} decrease after a lag time, which proportionally increases with the distance between the production well and the monitoring well. The lag time is associated with pressure diffusion. CO_2 will keep flowing upward until the underpressure imposed at the production well propagates to the monitoring location. For the CO_2 push-pull, the lag time is additionally affected by the strong buoyant rise of CO_2. The gas saturation at the monitoring locations decreases because CO_2 keeps flowing upward and exits the fault zone, not because it is recovered at the production well.

Note that Figure 6-4 includes as a comparison the pressure transient at MW_{200m} when water is used as an agent for the push-pull test (ΔP_w at MW_{200m}).

We assessed the sensitivity of pressure-transient and gas-saturation data to various model parameters and conditions using scaled sensitivity coefficients, which normalize sensitive coefficients by the a priori standard deviation of observation and the expected parameter variation. For both the push and pull periods, the pressure transient and gas saturation are most sensitive to the fault gouge permeability. The influence of the damage zone and matrix permeability on the pressure transient is minor, and on the gas saturation is even smaller since

CO_2 mainly flows through the fault gouge. Among different monitoring locations, the sensitivity is the strongest at MW_{200m}.

Figure 6-5 shows the scaled sensitivity of the pressure transient and gas saturation during the push period as a function of time. From early times of CO_2 injection, the pressure transient shows a significant sensitivity to fault gouge permeability (Figure 6-5a). On the other hand, the sensitivity of gas saturation (Figure 6-5b) is zero until the CO_2 plume reaches the monitoring location.

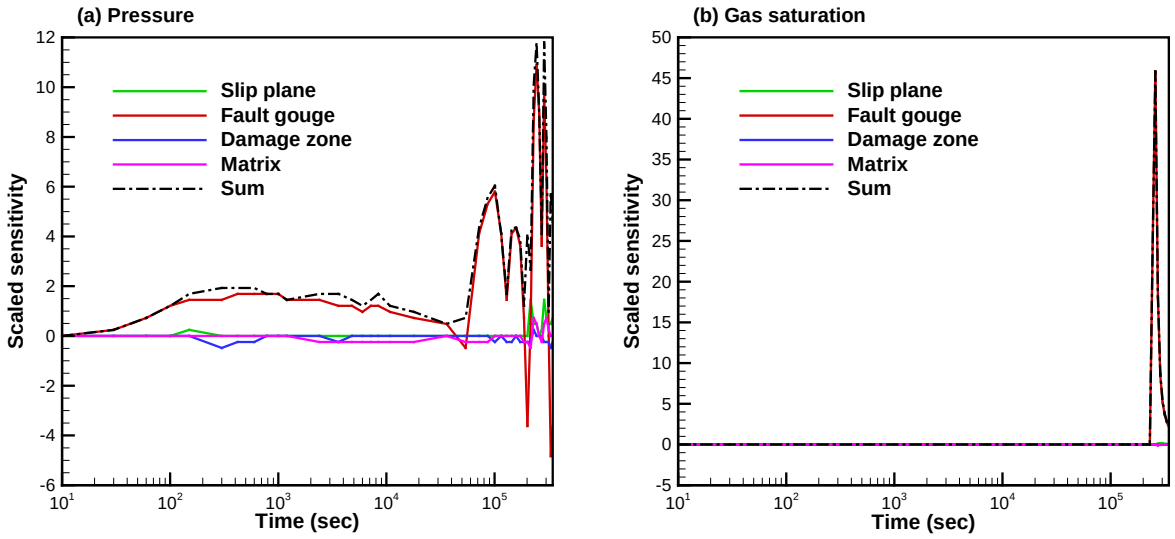

Figure 6-5. Temporal variation of the scaled sensitivity to material permeabilities: (a) pressure transient and (b) gas saturation.

To demonstrate the impact of material permeability on pressure transient, the pressure transients for different permeability conditions (varying the permeability of one material at a time) are plotted in Figure 6-6. The fault gouge permeability varies over one order of magnitude, whereas the damage zone and matrix permeability differ over two orders of magnitude.

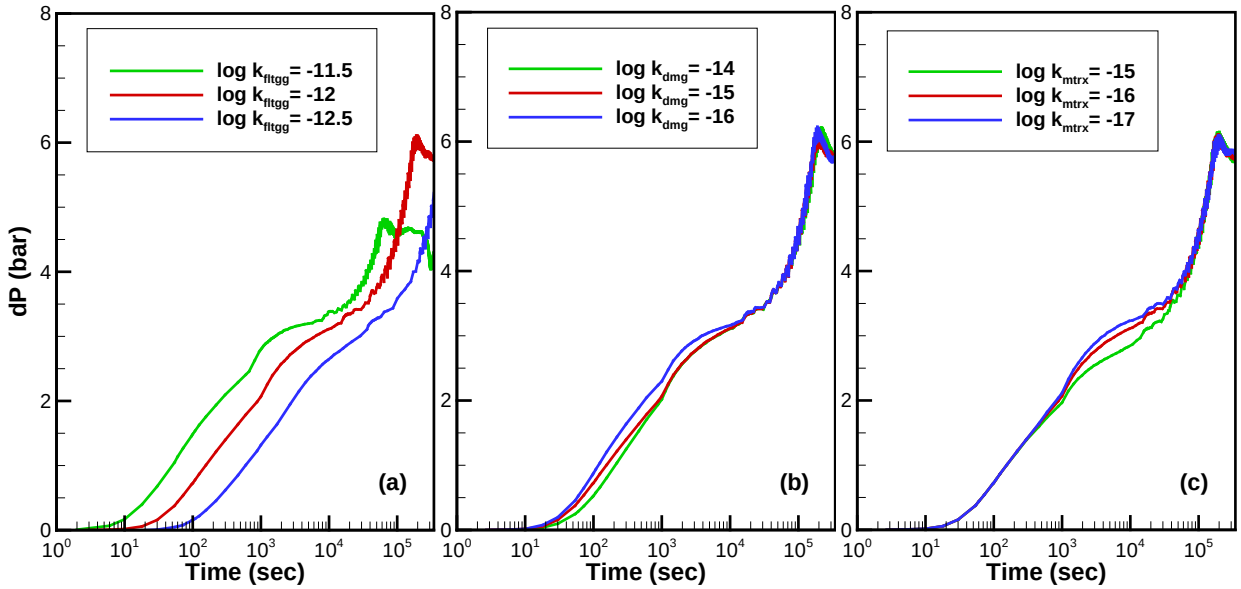

Figure 6-6. Pressure transients for different permeability conditions: (a) fault gouge, (b) damage zone, and (c) matrix.

To examine the effect of relative permeability and capillary functions on pressure transient and gas saturation data, we assessed the sensitivity to the multiphase flow parameters. The multiphase flow parameters are usually unknown at real EGS sites, and therefore it may be inevitable to have large uncertainties in these parameters. To examine the potential impact of the parameter uncertainty, we generated 50 sets of parameter combination using Latin Hypercube Sampling analysis (Zhang and Pinder, 2003) and simulated their impact on the pressure transient and gas saturation. Our Monte Carlo simulation results (Figure 6-7) showed that the pressure transient diverges soon after ~10^3 sec, when the CO_2 phase develops in the fault gouge, indicating that uncertainty in these multiphase flow parameters can significantly impair the accuracy of the fault characterization (i.e., calibrating the fault zone permeabilities). Results also showed that both the arrival time of the CO_2 plume and the level of gas saturation in the CO_2 plume can greatly vary depending on the parameter combination.

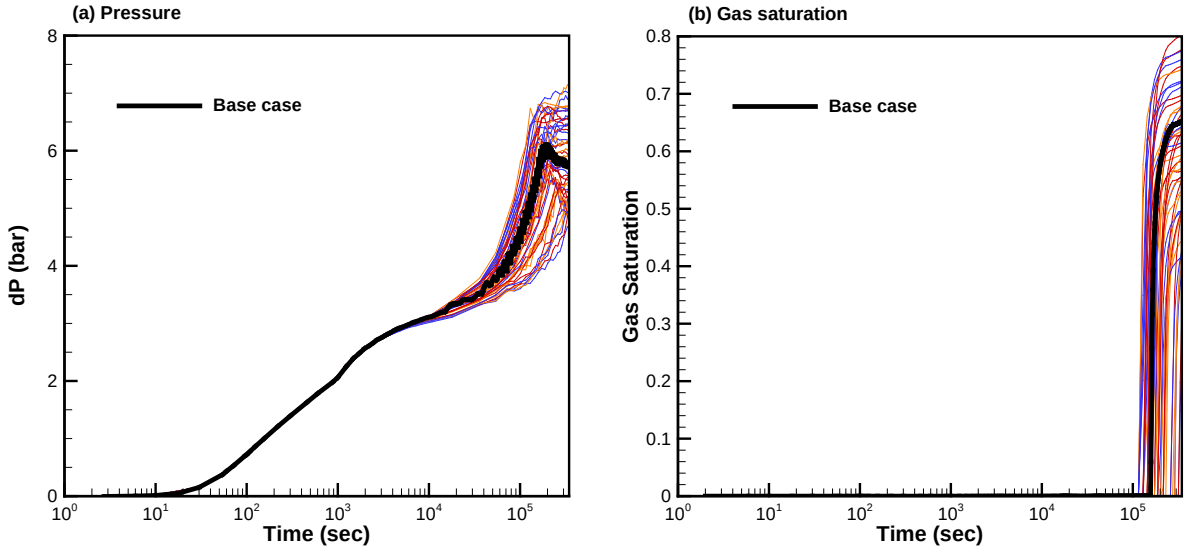

Figure 6-7. Monte Carlo uncertainty propagation analysis: (a) pressure transient and (b) gas saturation. The thick black line shows the base case, and the other thin lines with different colors represent Monte Carlo realizations.

Based on the sensitivity analysis results, we attempted fault characterization using synthetic data. The synthetic data for the push period are generated by running a forward simulation of the base case. We assumed that the permeability of the fault gouge, damage zone, and matrix are unknown, and considered two different inversion scenarios: (1) pressure transients only are available for inversion, and (2) both pressure transient and gas saturation data are available. Because the pressure transient is most sensitive to the fault gouge permeability, inversion is most accurate for estimating the fault gouge permeability.

6.3 Summary

To summarize our results, we observed that the modeled CO_2 mostly flows upward through the fault gouge and therefore the pressure transient mainly reflects the gouge properties such as gouge permeability. Consequently, the fault gouge permeability is most accurately estimated using the pressure transient data for inverse modeling. We also found that the local change in pressure at monitoring locations far above the injection point can be larger than the injection-induced pressure change at the injection well. This phenomenon occurs because of the gas column formed by the CO_2 and its lower density relative to brine. In short, the top of the gas column exerts its pressure on the water column in the fault zone above, and the associated overpressure exerted can be much larger than the injection overpressure itself.

7 SENSITIVITY AND DATA WORTH FOR A DUAL FAULT SYSTEM

7.1 Introduction

In this study, we developed a conceptual and numerical reservoir model of two intersecting faults based on the Dixie Valley geothermal system (DVGS) in Nevada, USA. The 2D conceptual model consists of a system with a main fault and an intersecting conjugate fault. The corresponding numerical model is discretized using irregular grid blocks with fine discretization

around the slip plane, gouge, and damage zones. We perform forward modeling along with sensitivity and data-worth analyses of $scCO_2$ push-pull to investigate the CO_2 distribution in the fault gouge during 30 days of push (injection) and 30 days of pull (production). Formal sensitivity analysis is conducted to determine the most controlling unknown parameters in the fault zones. Using the selected set of unknown parameters and output responses, we perform data-worth analysis to reveal the most valuable output response to be measured for the best prediction of CO_2 distribution in the fault zones and its uncertainty. From the results of data-worth analysis, we determine the optimal properties to target in monitoring, their locations, and the minimum observation time. Our results provide information on the optimal design of $scCO_2$ push-pull testing in a conjugate fault system modeled after Dixie Valley that can be used to enhance monitoring by active seismic and well-logging methods to better characterize the transmissive fault(s).

In this study, we investigate the technical feasibility of a $scCO_2$ push-pull test in the conjugate faults system of the geothermal resource at Dixie Valley in central Nevada, with temperature of the field is estimated to approach a 260 °C at a depth of 3 km (Blackwell et al., 2007; Iovenitti et al., 2016). In the forward modeling of $scCO_2$ push-pull in this study, we simulate the injection and production of $scCO_2$ into the junction of two conjugate faults. We also conduct a sensitivity analysis to evaluate the factors affecting CO_2 inflow into the faults and outflow from the faults. In addition, we conducted a data-worth analysis to predict the uncertainty of CO_2 distribution after the push and pull phases by measuring the system responses. In this procedure, the data worth of each measurement is computed to indicate the relative importance for the prediction of future system behavior. Additional results and details can be found in Lee et al. (2018).

7.2 Model system

A conceptual cross section of the DVGS (Figure 7-1) shows hot brine rising along the main faults giving rise to the isotherms shown in Figure 7-1 (Smith et al., 2011). This conceptual model is capture in our model domain as shown in Figure 7-2. Although the conceptual model is very simplified, it includes the essential components that affect flow of injected CO_2 and therefore retains the fundamental fault-flow-related aspects of the system.

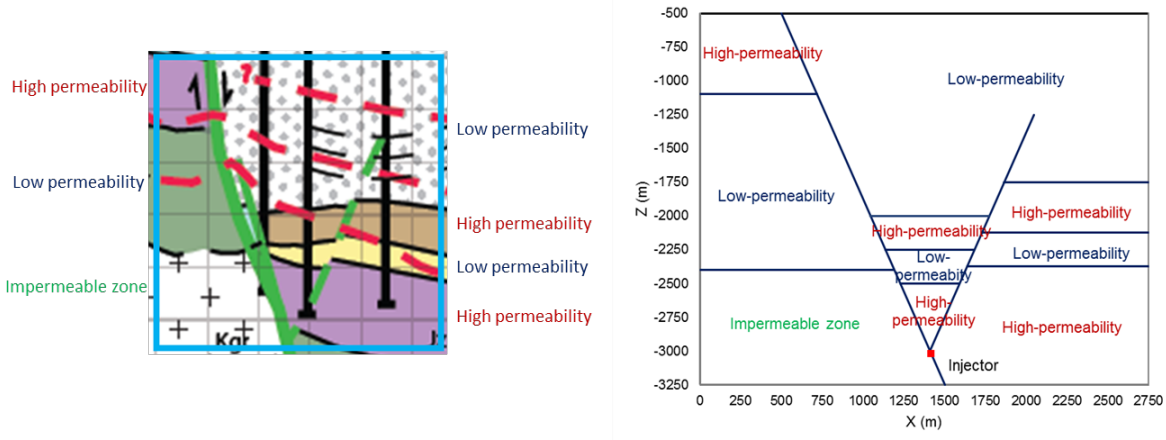

Figure 7-1. (a) Conceptual model of the 2D DVGS system. (b) Simplified model for simulating CO_2 push pull in a dual-fault system.

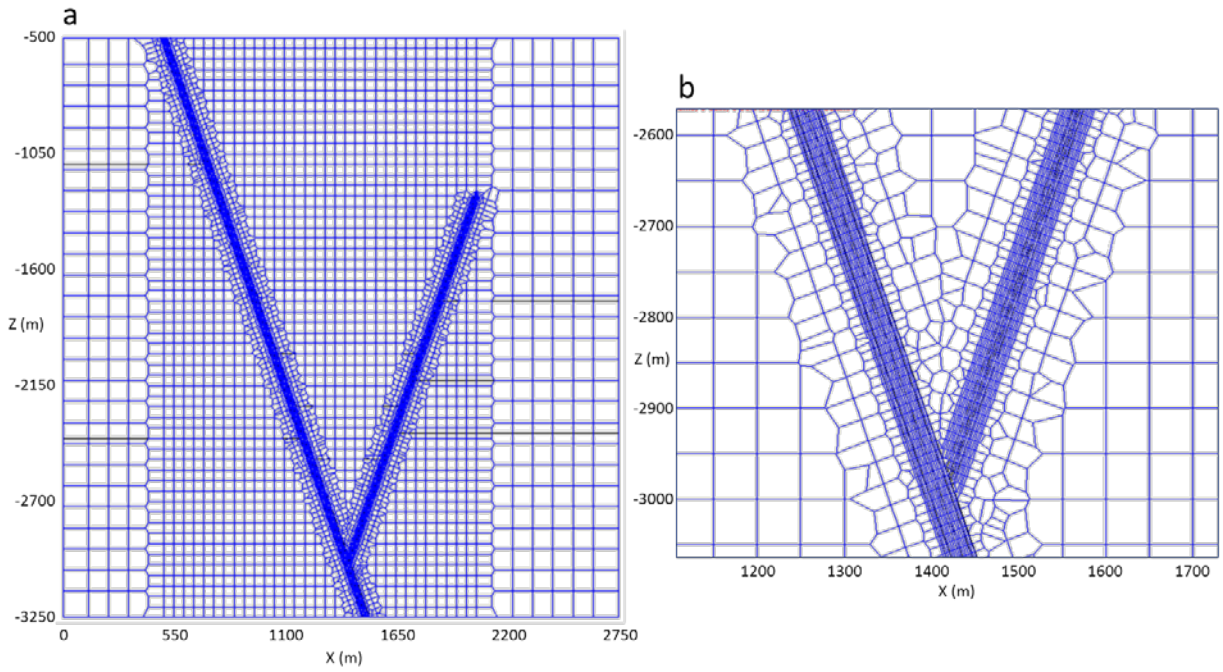

Figure 7-2. Grid geometry of the 2D conceptual model domain: (a) entire view, (b) expanded veiw at the junction of the two faults. Note that the horizontal black lines in (a) indicate the boundaries of different lithologic zones shown in Figure 7-1b.

Figure 7-3 shows the initial pressure and temperature distributions. The system is initially filled with brine; and a hydrostatic pressure gradient of 9.79 kPa/m is applied. The initial temperature distribution shows the effect of rising heat flow through the main fault, which was obtained by running a natural-state simulation. Constant pressure and temperature are set at the top boundary; and the other three sides are set at no flow condition of heat and fluid, in light of the short time of our push-pull test.

Hydrogeologic properties of the system for the numerical simulations are provided in Table 7-1. Potentially influential and unknown parameters for the flow of injected CO_2 in the fault zones are indicated with *—the absolute permeability, and the input parameters for the relative permeability and capillary pressure functions in the fault slip plane, fault gouge, and damage zone. Sensitivity and data-worth analyses will be performed for these parameters after the forward modeling section.

Table 7-1. Properties of the DVGS (Borgia et al., 2017a, b; Oldenburg et al., 2016). Rock grain density = 2650 kg·m^{-3}, pore compressibility = 7.25×10^{-12} Pa^{-1}, rock grain specific heat = 1000 J·kg^{-1}·K^{-1}, and formation thermal conductivity = 2.1 W·m^{-1}·K^{-1}, respectively. Note that $1/P_0$ is proportional to the square root of the absolute permeability.

Zone	Porosity [vol. frac.]	Permeability [m^2]	Parameters of capillary pressure	Parameters of relative permeability
Slip plane	0.30	2×10^{-12} *	None	Corey[2], S_{lr}* = 0.3; S_{gr}* = 0.05
Fault gouge	0.10	2×10^{-12} *	van Genuchten[1], λ* = 0.4438; S_{lr}* = 0.30; S_{ls} = 1.0; $1/P_0$* = 2.100×10^{-4} Pa^{-1}; P_{max} = 10^8 Pa	Corey[2], S_{lr}* = 0.3; S_{gr}* = 0.05
Damage zone	0.05	2×10^{-15} *	van Genuchten[1], λ* = 0.4438; S_{lr}* = 0.30; S_{ls} = 1.0; $1/P_0$* = 6.641×10^{-6} Pa^{-1}; P_{max} = 10^8 Pa	Corey[2], S_{lr}* = 0.3; S_{gr}* = 0.05
High-permeability zone	0.10	5×10^{-16}	van Genuchten[1], λ = 0.4438; S_{lr} = 0.30; S_{ls} = 1.0; $1/P_0$ = 3.321×10^{-6} Pa^{-1}; P_{max} = 10^8 Pa	Corey[2], S_{lr}* = 0.3; S_{gr}* = 0.05
Low-permeability zone	0.05	10^{-16}	van Genuchten[1], λ = 0.4438; S_{lr} = 0.30; S_{ls} = 1.0; $1/P_0$ = 1.485×10^{-6} Pa^{-1}; P_{max} = 10^8 Pa	Corey[2], S_{lr}* = 0.3; S_{gr}* = 0.05
Impermeable zone	0.01	10^{-19}	van Genuchten[1], λ = 0.4438; S_{lr} = 0.30; S_{ls} = 1.0; $1/P_0$ = 4.696×10^{-8} Pa^{-1}; P_{max} = 10^8 Pa	Corey[2], S_{lr}* = 0.3; S_{gr}* = 0.05

[1]van Genuchten, 1980, [2]Corey, 1954

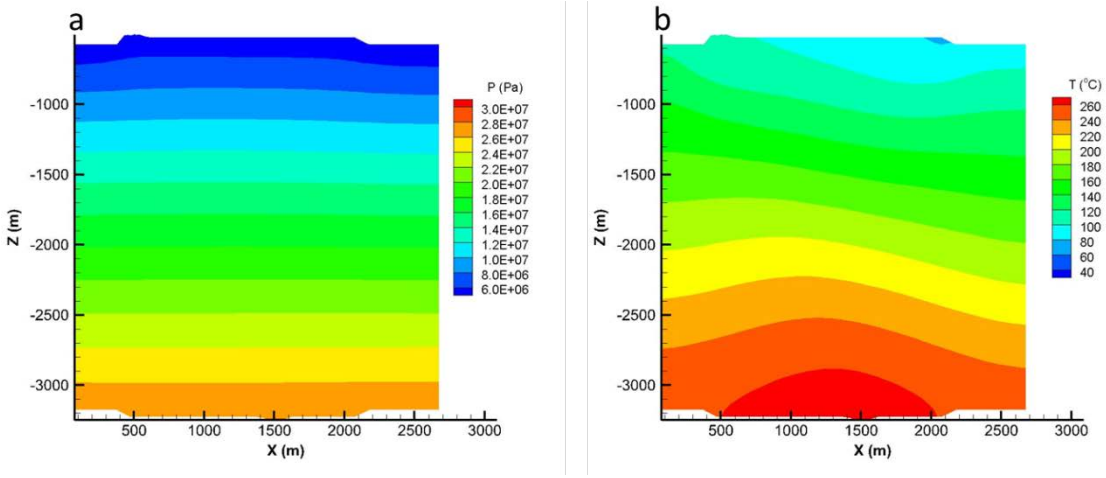

Figure 7-3. Reservoir initial conditions: (a) pressure distribution, (b) temperature distribution.

In the push phase, CO_2 was injected by using a 0.3 MPa constant overpressure above the local hydrostatic pressure in the injection grid blocks in the fault slip plane and fault gouge of the main fault at *z*-coordinates between -3018 m and -3024 m, which is just below the junction of the main and conjugate faults. Temperature of injected CO_2 was same as the local ambient temperature of 265 °C. In the pull phase, fluid was produced by 0.3 MPa underpressure at the same locations as the injection.

Results of numerical simulations are provided in Figure 7-4 which shows the distribution profiles of pressure, temperature, and gas saturation in the reservoir, after push (a-c) and pull processes (d-f). After the 30 days of push, the system pressure slightly increased along the faults (Figure 7-4a). Similarly, system pressure slightly decreased along the faults after the subsequent 30-day pull process (Figure 7-4d). System temperature insignificantly changed in the faults after the push and pull, as the CO_2 was injected at the ambient temperature (Figure 7-4b and e).

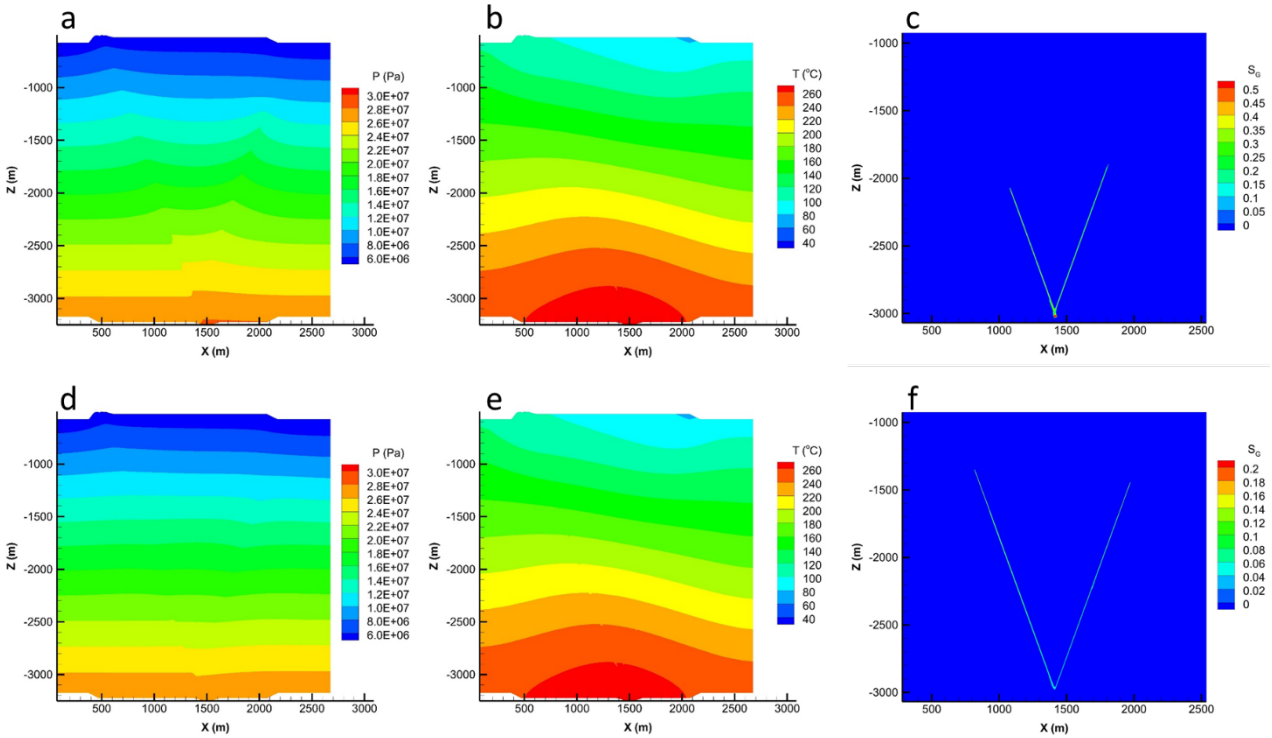

Figure 7-4. Reservoir profiles after 30 days-push and following 30 days of pull: (a) pressure distribution after push, (b) temperature distribution after push, (c) gas saturation distribution after push, (d) pressure distribution after pull, (e) temperature distribution after pull, (f) gas saturation distribution after pull. Note that in the plots of gas saturation distributions (c) and (f), different extents of the domain (different *X* and *Z* limits) were used relative to those for the pressure and temperature plots.

The gas saturation profiles in Figure 7-4c show that the injected CO_2 reached upward to Z = -2070 m and -1890 m in the main and conjugate faults, respectively, i.e., reached a higher level in the smaller conjugate fault. Injected CO_2 flowed upward more easily in the conjugate fault than in the main fault because the conjugate fault contacts formations with high permeability over a larger surface area than the main fault does, as shown in Figure 7-1b, providing less resistance for water in the conjugate fault to flow into the formation as it is displaced by CO_2.

After the pull phase, CO_2 had risen by buoyancy to Z = -1345 m and -1440 m in the main and conjugate faults, respectively (Figure 7-4f). CO_2 still flowed upward in the early time period of the pull phase in both the conjugate and main faults, and slightly flowed down afterward. Overall, the fluid flowing in the faults during both the push and pull phases consisted mainly of water, with only a small amount of CO_2 in the six order of magnitude smaller than the mass flow of water.

We observed the pressure, temperature, and saturation of gaseous phase in the gouge of fault zones, where the most injected CO_2 passed along during push and pull. The observation positions

are at three different locations at Z = -2925 m, -2520 m, and -2100 m in the main and conjugate faults. The observation results are shown in Figures 7-5–7-7. Note that pressure in the fault zones promptly reacted to the injection and production of CO_2, while temperature and saturation of gaseous phase reacted slower than pressure did.

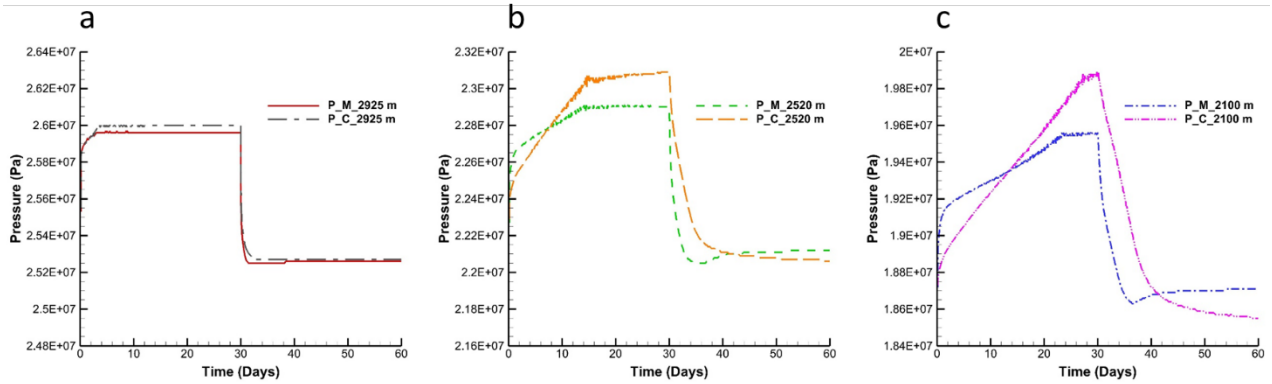

Figure 7-5. Observed pressure as a function of time at three different locations in the main and conjugate faults: (a) Z = -2925 m, (b) Z = -2520 m, (c) Z = -2100 m.

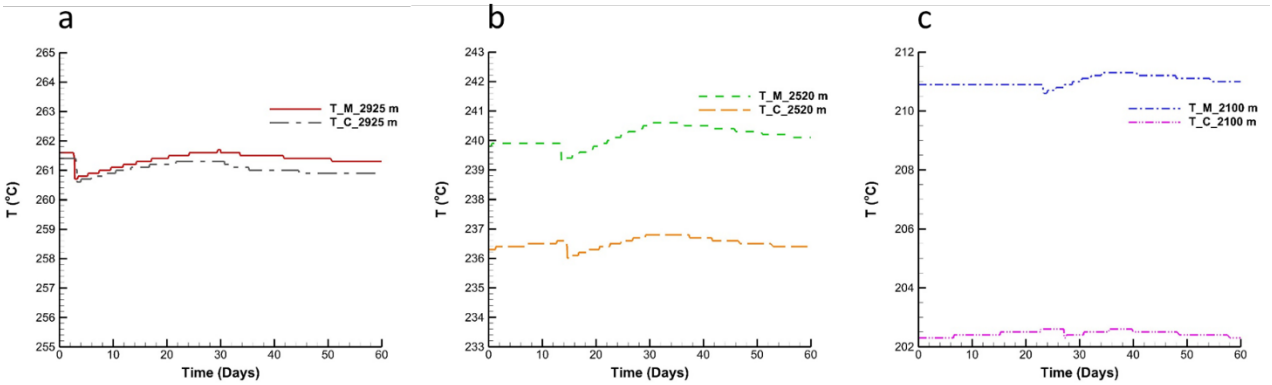

Figure 7-6. Observed temperature as a function of time at three different locations in the main and conjugate faults: (a) Z = -2925 m, (b) Z = -2520 m, (c) Z = -2100 m.

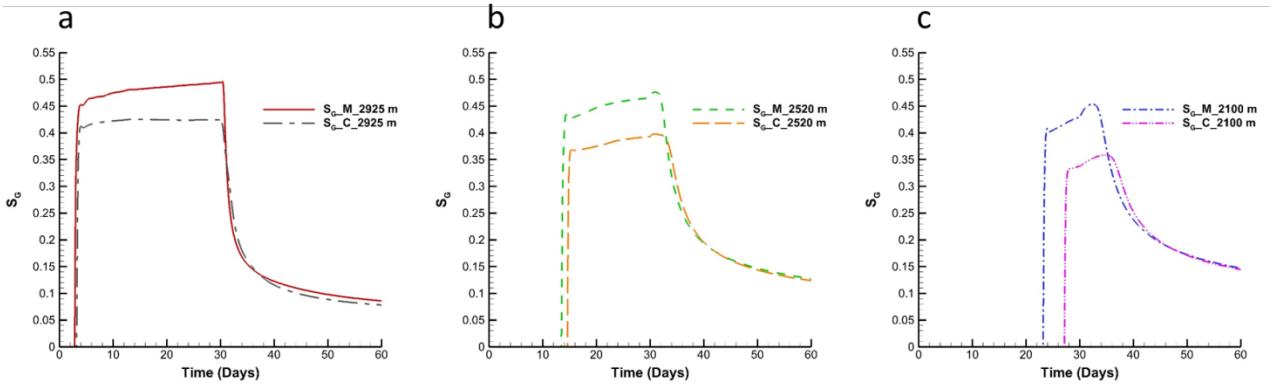

Figure 7-7. Observed gaseous phase saturation as a function of time at three different locations in the main and conjugate faults: (a) Z = -2925 m, (b) Z = -2520 m, (c) Z = -2100 m.

We carried out a data worth analysis to guide potential monitoring that would be done in a field deployment of CO_2 push-pull. The approach was to perturb the five most-controlling unknown parameters in each of the push and pull phases

- Push: slip plane (S_{gr}), fault gouge (λ, $1/P_0$, S_{lr}, S_{gr})
- Pull: slip plane (S_{gr}), fault gouge ($1/P_0$, S_{gr}), damage zone (K, S_{gr})

for 30 days of CO_2 injection, followed by observation for 20 days of the 12 measurable responses

- Pressure (main & conjugate fault @ 2925, 2520, 2100 m)
- Temperature (main & conjugate fault @ 2925, 2520, 2100 m)

Then we predict the CO_2 distributions in the fault zones after 30 days of pull

- S_G at main & conjugate fault @ 2925, 2520, 2100 m)

The results are shown in Figure 7-8. In the push phase, PM_2520 m showed the highest data worth for reducing prediction uncertainty, followed by PC_2520 m, PC_2100 m, and PM_2100 m. By summing up the data-worth values, we found that the measurement of these four observation data reduced the prediction uncertainly by 86.45%. In addition to these four observations, measurement of PM_2925 m reduced the prediction uncertainty even more. The measurement of temperature was not necessarily recommended for the reduction of prediction uncertainty, owing to their low data-worth values. The reason for this result is the much higher sensitivity coefficients of pressure than temperature, which arise because of the faster and more active response of pressure relative to temperature during the push process.

In the pull phase, PC_2100 m showed the highest data worth, followed by PM_2100 m, PC_2520 m, and PM_2520 m. The measurement of these four observation data reduced the prediction uncertainly by 99.97%. Other measurement data showed insignificant data worth below 0.01%.

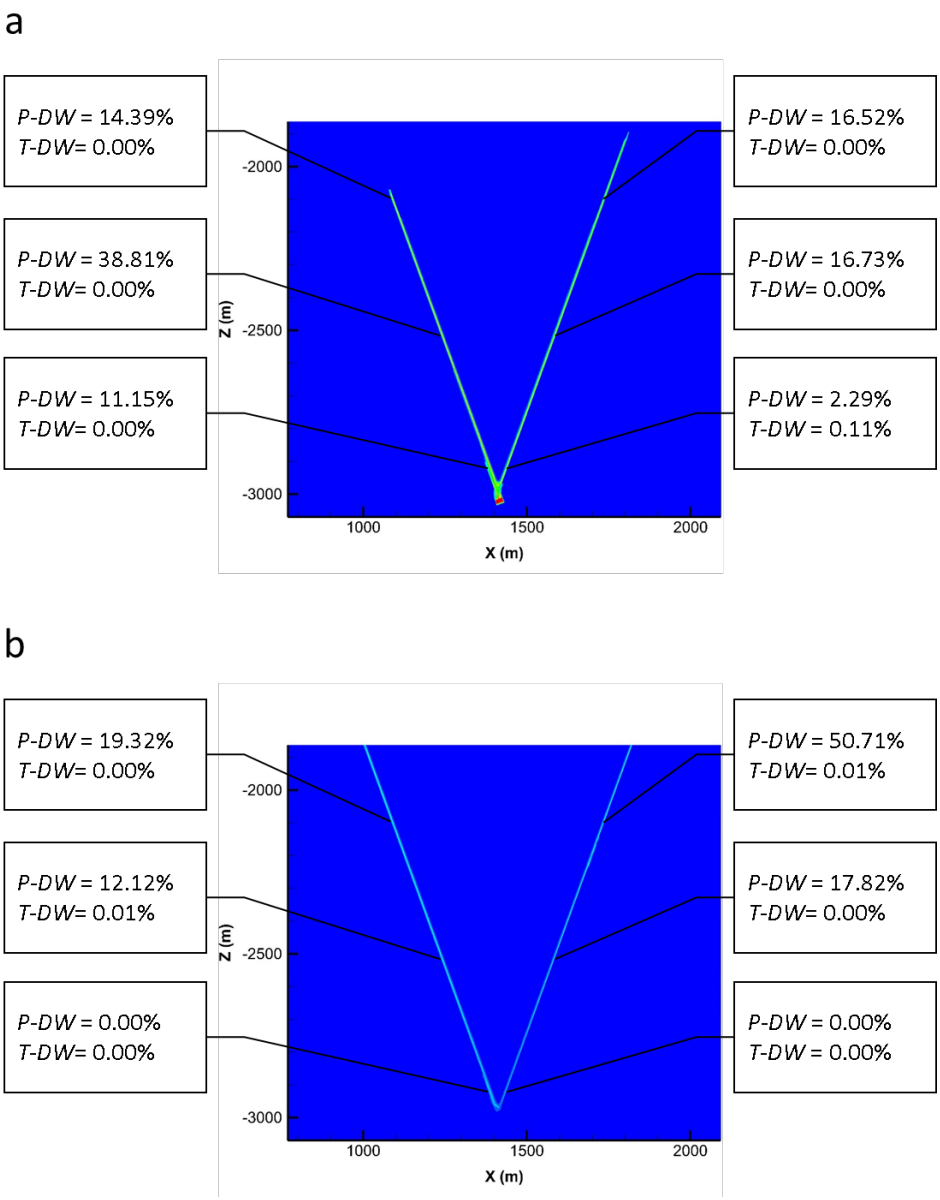

Figure 7-8. Data worth values at each observation point: (a) in push phase, (b) in pull phase. The plots of domain were obtained from the profiles of gas saturation distributions after push and pull, respectively.

7.3 Summary

Along with forward simulations, we performed sensitivity analysis and data-worth analysis. From the formal sensitivity analysis, we determined the most influential parameters in the fault zones on the measureable system responses such as pressure and temperature, and the most sensitive system responses among them. From the data-worth analysis, we determined the most valuable observation data to be measured for the best prediction of CO_2 distribution in the faults. These results can be used to guide field monitoring efforts to measure CO_2 saturation in order to calibrate and constrain active seismic monitoring used to characterize the extent and properties of fault zones relevant to EGS objectives.

Although this study was carried out in an idealized 2D model system, the approach we describe is applicable to any system and can be used to design monitoring approaches to collect the most valuable data. These data can then be used to make point measurements to calibrate and constrain active seismic, well logging, or other monitoring data collected in campaigns aimed at better characterizing permeable faults and fractures critical for EGS.

8 DISCUSSION

In the course of this project, we have carried out a range of modeling and simulation activities directed at evaluating the technical feasibility of using CO_2 injection (and withdrawal) to enhance characterization of permeable fault systems. While our conclusions are only as valid as our simulations, and our simulations are simplified and based on prototypical systems, our results suggest that there is promise in this approach. In short, we demonstrated that

- CO_2 largely confines itself to the more-permeable fault zone (gouge) region upon injection,
- CO_2 creates changes in neutron capture cross section that can be detected by well logging,
- CO_2 causes changes in elastic properties that may be detected by time-lapse active seismic approaches,
- Pressure-transient analysis during CO_2 injection can provide information about fault gouge properties, and
- Simulations of CO_2 pressure and saturation changes can be used to develop information on where to most optimally make measurements of various kinds for optimal characterization.

Although the results were overall promising, they showed the CO_2 push-pull concept is far from a proven technology. First, we found early in the project that isolated fractures, or systems with large fracture spacing, would not show significant time-lapse changes in either well logging or active seismic time-lapse monitoring, so we focused on faults which have a wider zone of potential permeation by CO_2. Although not studied explicitly here, we expect fracture, or shear, zones of similar cumulative thickness to our prototypical fault zone to also be promising targets for CO_2 push-pull-based enhanced characterization.

Second, within the fault zone system studied, we found that CO_2 withdrawal (pull) is very limited because of buoyancy which causes the CO_2 to flow upward out of the capture zone of the pull cycle. Although this negates the CO_2 pull part of push-pull, the withdrawal of water during the pull period provides an effective perturbation for pressure-transient analysis, and may even provide some benefits by stressing different parts of the system than during CO_2 withdrawal.

Third, well logging shows promise for saturation-based changes (conductivity and neutron capture), but non-feasibility for density or elastic-property-based approaches. One interesting finding along these lines is that dynamic range calculations of well logging show good sensitivity to CO_2 saturation, but the actual saturation changes expected and observed in our simulations make well logging tools based on elastic properties appear non-feasible. The conclusion that acoustic methods are unlikely to be successful would seem to rule out seismic imaging. But we

note that the well-logging feasibility analyses assume homogeneous rock around the well and the acoustic logging only samples a small region around the well. In contrast, field-scale active seismic monitoring interrogates a larger and more heterogeneous region of varying geometry that can enhance the contrast provided by injected CO_2.

Fourth, simulation of seismic monitoring and CO_2 injection are computationally intensive activities requiring more resources than were available in this project. For example, we limited most of our analyses to 2D systems to make run-times and data handling practical. In addition, full wave-form inversion was deemed too intensive leading us to choose reverse time migration as a more practical seismic inversion approach. Similarly, we defined a simple 2D prototypical EGS system to focus on, but clearly 3D systems with greater realism should be considered in future work in this area.

Overall, the results of our modeling- and simulation-based feasibility study show CO_2 push-pull to be promising, and that further work is warranted as described in the next section.

9 FUTURE WORK

9.1 Field demonstration

We believe additional work in this area is warranted based on (1) the promising results of this study, and (2) the high pay-off for EGS site characterization if gas-phase push-pull can be developed into a reliable characterization method. As a first step toward field validation of these results, we developed a draft field test plan (see Appendix I). If a specific site were to be selected, we would recommend investing in 3D modeling to confirm the expected response, as discussed below.

9.2 Modeling and Simulation

The modeling and simulation in this study were in three main areas: (1) hydrologic modeling of non-isothermal CO_2 and water push-pull with extensions to inverse modeling and data-worth analysis; (2) modeling of well logging; and (3) modeling of active seismic monitoring. There are several extensions and improvements that should be made in future research in this area.

First, modeling and simulation should be extended to three dimensions. For our purposes in establishing a proof of principle and preliminary simulation-based demonstration, 2D modeling was sufficient. But for refinement of the analysis and design of field experiments, 3D modeling of the push-pull and the active seismic monitoring should be undertaken. In addition, more realistic fault zone and/or fracture zone characteristics are needed to improve modeling and simulation (see Section 1.9.3).

Second, more research should be carried out in understanding changes in bulk rock elastic properties as a function of CO_2 saturation and saturation patterns, for example refinements of the Gassmann and patchy saturation models. Laboratory efforts are needed in this area, but so are defensible up-scaling approaches to understand large-scale injection and its impacts on active seismic monitoring.

Third, the CO_2 push-pull approach proposed here relies ultimately on inverting observations of *P*, *T*, and saturation, well logging, and active seismic monitoring. Joint inversion is the natural approach to making optimal use of all of the data available. Yet joint inversion of multiple data

streams and types is still a daunting computational task. More research should be carried out to develop joint inversion as a practical and widely used method to maximize return on monitoring investments.

9.3 Fault and Fracture Properties

Fault property characterization and/or generalization is an unmet need relevant to many fields, e.g., contaminant flow and transport, oil and gas production, subsurface energy and fuel storage, geologic carbon sequestration, and EGS. Simply put, we need to know more about fault properties, fault zones, and fracture properties and fracture zone properties. Ideally, a comprehensive data mining of published literature and field experiences across the full spectrum of subsurface endeavors would be undertaken to organize and comprehend fault properties. For practicality, a more compact version of such a study should be undertaken for EGS given the smaller range of relevant lithologies and more tractable amount of data and literature available for EGS. Scientific drilling of faults in geothermal fields is the optimal way to extend current knowledge.

9.4 High-Quality Active Seismic Data Acquisition

As demonstrated in this study, active seismic imaging of CO_2 in the fault gouge will require high-quality seismic data, i.e., data with minimal noise. Study should be aimed at optimal geometries and instrumentation deployment strategies to generate the kinds of low-noise data needed to exploit the small changes in signal that are expected to arise from fluid displacement in EGS faults by gases such as CO_2. It is likely that any EGS project will require a larger effort in seismic acquisition and processing than comparable oil and gas fields due to the subsurface complexity.

9.5 Integration with waterless (CO_2-based) stimulation

For a variety of reasons summarized by Moridis (2017), there is growing interest in the U.S. in waterless stimulation, e.g., CO_2-based fracturing. Insofar as monitoring and characterizing active stimulation processes in near-real time are desirable, the present push-pull analyses are directly applicable. Simply put, the injected CO_2 may produce a property anomaly relative to the pre-stimulation characteristics that is sufficient to image in a time-lapse manner the formation and growth of the fractures. The pressure-transient analysis of the fracture fluid (CO_2) injection and flow back (CO_2 and water) would also provide information on the fracturing and overall reservoir characteristics. Our results to date suggest that small fractures filled with CO_2 will be difficult to detect in crystalline rock, but a more thorough study spanning the parameter space relevant to EGS including deep shale prospects seems warranted to assess the likelihood of this approach being successful for characterizing waterless induced fracture systems in near-real time.

10 CONCLUSIONS

We have carried out an initial modeling and simulation study to investigate the technical feasibility of injecting CO_2 into fault zones at EGS sites to enhance geophysical contrast to improve monitoring that can be used to better characterize the fault zone. Simulations of the

injection of CO_2 show that gravity effects cause the CO_2 to preferentially flow up the hanging wall in the gouge zone of a dipping fault. Simulation of active seismic monitoring of this CO_2 shows small time-lapse changes that encourage further study and motivate improvements in signal-to-noise ratio for seismic detection, and encourage the use of a crosswell configuration to enhance the seismic detection of the CO_2. Modeling of active crosswell seismic monitoring suggests contrasts that may be feasible for better characterization of zones into which CO_2 flows. Neutron capture well logging appears to be very capable of detecting and characterizing the saturation distribution of CO_2 in the fault gouge. Complementing these geophysical methods are pressure-transient and data-worth analyses which show that pressure monitoring at specific locations provides optimal data for characterizing fault gouge permeability. Further details of work in this project can be found in publications and conference proceedings.

11 ACKNOWLEDGMENTS

Support for this work was provided by the Office of Energy Efficiency and Renewable Energy, Geothermal Technologies Office, U.S. Department of Energy. Additional support was provided by the Assistant Secretary for Fossil Energy (DOE), Office of Coal and Power Systems, through the National Energy Technology Laboratory (NETL), by Lawrence Berkeley National Laboratory under Department of Energy Contract No. DE-AC02-05CH11231, and by EDRA. Pre- and post-processing of TOUGH2 simulations is done using a free GMS license provided by Acquaveo™.

12 REFERENCES

Altundas, Y., Chugunov, N., and Ramakrishnan, T. S., 2013. On the importance of accurate CO2 fluid and fluid substitution models for the seismic monitoring of CO2. SEG Technical Program Expanded Abstracts 2013: pp. 2716-2721.

Baysal et al., 1983, Baysal, E., Kosloff, D., and Sherwood, J.W.C., 1983, Reverse time migration: Geophysics, 48, 1514–1524.

Blackwell, D.D., Smith, R.P. and Richards, M.C., 2007. Exploration and development at Dixie Valley, Nevada: Summary of DOE studies, Proceedings, 32nd Workshop of Geothermal Reservoir Engineering, pp. 16.

Borgia, A., Oldenburg C.M., Zhang R., Jung Y., Lee K.J., Doughty C., Daley T.M., Altundas B., Chugunov N., Ramakrishnan T.S., 2017a. Simulations of Carbon Dioxide Injection, Seismic Monitoring, and Well Logging for Enhanced Characterization of Faults in Geothermal Systems. PROCEEDINGS, 42nd Workshop on Geothermal Reservoir Engineering Stanford University, Stanford, California, February 13-15, SGP-TR-212.

Borgia, A., Oldenburg C.M., Zhang R., Pan L., Daley T.M., Finsterle S., Ramakrishnan T.S., 2017b. Simulation of CO_2 injection into fractures and faults for improving their geophysical characterization at EGS Sites. Geothermics, v. 69, p. 189-201, http://dx.doi.org/10.1016/j.geothermics.2017.05.002.

Borgia, A., Oldenburg C.M., Zhang R., Pan L., Finsterle S., Ramakrishnan T.S., 2015. Simulations of CO_2 push-pull in fractures to enhance geophysical contrast for characterizing EGS sites. PROCEEDINGS, TOUGH Symposium 2015, Lawrence Berkeley National Laboratory, Berkeley, California, September 28-30, p. 109-115.

Borgia, A., Pruess, K., Kneafsey, T.J., Oldenburg, C.M., Pan, L., 2013. Simulation of CO_2-EGS in a fractured reservoir with salt precipitation. Energy Procedia, 37, 6617-6624, doi:10.1016/j.egypro.2013.06.594.

Chugunov N., Altundas Y. B., Ramakrishnan T. S., and Senel, O., 2013. Global sensitivity analysis for crosswell seismic and nuclear measurements in CO_2 storage projects. Geophysics, 78 (3): WB77–WB87. http://dx.doi.org/10.1190/geo2012-0359.1

Coates, R., Schoenberg, M., 1995. Finite difference modeling of faults and fractures. GEOPHYSICS 60(5), 1514–1526. URL http://dx.doi.org/10.1190/1.1443884

Corey, A.T., 1954. The interrelation between gas and oil relative permeabilities. Producers monthly, 19(1), pp.38-41.

Daley, T.M., Schoenberg, M.A., Rutqvist, J., Nihei, K.T., 2006, Fractured reservoirs: An analysis of coupled elasto-dynamic and permeability changes due to pore pressure variation, Geophysics, v71, n5, O33-O41.

Daley, T.M., Myer, L.R., Peterson, J.E., Majer, E.L., Hoversten, G.M., 2008, Time-lapse crosswell seismic and VSP monitoring of injected CO2 in a brine aquifer, Environmental Geology, 54, 1657-1665, DOI:10.1007/s00254-007-0943-z.

Etgen, J., 1987. Finite difference elastic anisotropic wave propagation.

Faulds, J., Moeck, I., Drakos, P., Zemach, E., 2010a. Structural Assessment and 3D geologic modeling of the Brady's geothermal area, Churchill County (Nevada, USA): A preliminary report. In: 35st Workshop on Geothermal Reservoir Engineering. pp. 298–302.

Faulds, J.E., Coolbaugh, M.F., Benoit, D., Oppliger, G., Perkins, M., Moeck, I. and Drakos, P., 2010b. Structural controls of geothermal activity in the northern Hot Springs Mountains, western Nevada: The tale of three geothermal systems (Brady's, Desert Peak, and Desert Queen). Geothermal Resources Council Transactions, 34, pp.675-683.

Faulds, J.E., and Garside, L.J. 2003. Preliminary geologic map of the Desert Peak – Brady geothermal fields, Churchill County, Nevada, Nevada Bureau of Mines and Geology Open-File Report 03-27.

Finsterle S. and Y. Zhang, 2011. Solving iTOUGH2 simulation and optimization problems using the PEST protocol. Environ Modell Softw, 26(7), 959–968. http://dx.doi.org/10.1016/j.envsoft.2011.02.008.

Finsterle, S., 1993. ITOUGH2 users guide version 2.2 (No. LBL--34581). Lawrence Berkeley Lab., CA (United States).

Finsterle, S., 2004. Multiphase inverse modeling: review and iTOUGH2 applications. Vadose Zone Journal, 3, 747–762.

Finsterle, S., M. Commer, J. Edmiston, Y. Jung, M.B. Kowalsky, G.S.H. Pau, H. Wainwright, and Y. Zhang, 2016. iTOUGH2: A simulation-optimization framework for analyzing multiphysics subsurface systems, Computers and Geosciences, https://doi.org/10.1016/j.cageo.2016.09.005.

Genter, A., Evans, K., Cuenot, N., Fritsch, D. and Sanjuan, B., 2010. Contribution of the exploration of deep crystalline fractured reservoir of Soultz to the knowledge of enhanced geothermal systems (EGS). Comptes Rendus Geoscience, 342(7), pp.502-516.

Gudmundsson, A., Fjeldskaar, I. and Brenner, S.L., 2002. Propagation pathways and fluid transport of hydrofractures in jointed and layered rocks in geothermal fields. Journal of Volcanology and Geothermal Research, 116(3), pp.257-278.

Harris, J. M., NolenHoeksema, R. C., Langan, R. T., Schaack, M. V., Lazaratos, S. K., James W. Rector, I., 1995. Highresolution crosswell imaging of a west texas carbonate reservoir: Part 1project summary and interpretation. GEOPHYSICS 60(3), 667–681. URL https://doi.org/10.1190/1.1443806

Iovenitti, J., Ibser, F.H., Clyne, M., Sainsbury, J. and Callahan, O., 2016. The Basin and Range Dixie Valley Geothermal Wellfield, Nevada, USA—A test bed for developing an Enhanced Geothermal System exploration favorability methodology. Geothermics, 63: 195-209.

Jung, Yoojin, Christine Doughty, Andrea Borgia, Kyung Jae Lee, Curtis M. Oldenburg, Lehua Pan, Thomas M. Daley, Rui Zhang, Bilgin Altundas, Nikita Chugunov, T.S. Ramakrishnan, Pressure transient analysis during CO_2 push-pull tests into faults for EGS characterization, in review.

Komatitsch, D. and Martin, R., 2007. An unsplit convolutional perfectly matched layer improved at grazing incidence for the seismic wave equation. Geophysics, 72(5), pp.SM155-SM167.

Lazaratos, S. K., Harris, J. M., James W. Rector, I., Schaack, M. V., 1995. Highresolution crosswell imaging of a west texas carbonate reservoir: Part 4reflection imaging. GEOPHYSICS 60(3), 702–711. https://doi.org/10.1190/1.1443809

Lee, Kyung Jae, Curtis M. Oldenburg, Christine Doughty, Yoojin Jung, Andrea Borgia, Lehua Pan, Rui Zhang, Thomas M. Daley, Bilgin Altundas, and Nikita Chugunov, Simulations of Carbon Dioxide Push-Pull into a Conjugate Fault System Modeled after Dixie Valley—Sensitivity Analysis of Significant Parameters and Uncertainty Prediction by Data-Worth Analysis, Geothermics, in press.

Lutz, S., Moore, J., Jones, C., Suemnicht, G. and Robertson-Tait, A., 2009. Geological and structural relationships in the Desert Peak Geothermal System, Nevada: Implications for EGS development. In Proceedings 34th Workshop on Geothermal Reservoir Engineering.

Madariaga, R., 1976. Dynamics of an expanding circular fault. Bulletin of the Seismological Society of America 66(3), 639–666. URL http://www.bssaonline.org/content/66/3/639.abstract

Majer, E.L., Peterson, J.E., Daley, T., Kaelin, B., Myer, L., Queen, J., D'Onfro, P. and Rizer, W., 1997. Fracture detection using crosswell and single well surveys. Geophysics, 62(2), pp.495-504.

Martin, R., Komatitsch, D. & Ezziani, A., 2008a. An unsplit convolutional perfectly matched layer improved at grazing incidence for seismic wave equation in poroelastic media, Geophysics, 73(4), T51–T61.

Martin, R., Komatitsch, D. & Gedney, S.D., 2008b. A variational formulation of a stabilized unsplit convolutional perfectly matched layer for the isotropic or anisotropic seismic wave equation, Comput. Modell. Eng. Sci., 37(3), 274–304.

Martin, R., Komatitsch, D., 2009. An unsplit convolutional perfectly matched layer technique improved at grazing incidence for the viscoelastic wave equation. Geophysical Journal International 179(1), 333–344.

McKeon, D.C. and H.D. Scott, 1989, SNUPAR - a nuclear parameter code for nuclear geophysics applications: Nuclear Science, IEEE Transactions, 36, no. 1, 1215-1219, doi: 10.1109/23.34634

Moridis, G.J., 2017. Literature Review and Analysis of Waterless Fracturing Methods, LBNL publications archive, https://pubarchive.lbl.gov/islandora/object/ir%3A1007287/datastream/PDF/view

Nakagawa, S. and Schoenberg, M.A., 2007. Poroelastic modeling of seismic boundary conditions across a fracturea). The Journal of the Acoustical Society of America, 122(2), pp.831-847.

Nemat-Nasser, S., Hori, M., 1999. Micromechanics: overall properties of heterogeneous materials. Vol. 2. Elsevier Amsterdam.

NolenHoeksema, R. C., Wang, Z., Harris, J. M., Langan, R. T., 1995. Highresolution crosswell imaging of a west texas carbonate reservoir: Part 5core analysis. GEOPHYSICS 60(3), 712–726. URL https://doi.org/10.1190/1.1443810

Oldenburg, C.M., Daley, T.M., Borgia, A., Zhang, R., Doughty, C., Ramakrishnan, T.S., Altundas, B., Chugunov, N., 2016. Preliminary Simulations of Carbon Dioxide Injection and Geophysical Monitoring to Improve Imaging and Characterization of Faults and Fractures at EGS Sites. PROCEEDINGS, 41st Workshop on Geothermal Reservoir Engineering, Stanford University, Stanford, California, February 22-24, 2016, SGP-TR-209.

Pan, L., Spycher, N., Doughty, C. and Pruess, K., 2014. ECO2N V. 2.0: A New TOUGH2 Fluid Property Module for Mixtures of Water, NaCl, and CO_2 (No. LBNL-6930E). Ernest Orlando Lawrence Berkeley National Laboratory, Berkeley, CA (US).

Pan, L., Spycher, N., Doughty, C. and Pruess, K., 2016. ECO2N V2.0: A TOUGH2 fluid property module for modeling CO_2-H_2O-NaCL systems to elevated temperatures of up to 300°C. Greenshouse Gases Science and Technology. DOI: 10.1002/ghg.1617.

Pruess, K., C.M. Oldenburg, and G.J. Moridis. TOUGH2 User's Guide Version 2. E. O. Lawrence Berkeley National Laboratory Report LBNL-43134, 1999; and LBNL-43134 (revised), 2012.

Rector, J.W., I., Lazaratos, S. K., Harris, J. M., Schaack, M. V., 1995. Highresolution crosswell imaging of a west texas carbonate reservoir: Part 3wavefield separation of reflections. GEOPHYSICS 60(3), 692–701. URL https://doi.org/10.1190/1.1443808

Roden, J.A. and Gedney, S.D., 2000. Convolutional PML (CPML): An efficient FDTD implementation of the CFS-PML for arbitrary media. Microwave and optical technology letters, 27(5), pp.334-338.

Schaack, M. V., Harris, J. M., James W. Rector, I., Lazaratos, S., 1995. Highresolution crosswell imaging of a west texas carbonate reservoir: Part 2wavefield modeling and analysis. GEOPHYSICS 60 (3), 682–691. URL https://doi.org/10.1190/1.1443807

Smith, R.P., Breckenridge, R.P. and Wood, T.R., 2011. Preliminary Assessment of Geothermal Resource Potential at the UTTR, Idaho National Laboratory (INL).

Snir, M., Otto, S., Huss-Lederman, S., Walker, D., Dongarra, J., 1998. MPI- The Complete Reference, Volume 1: The MPI Core, 2nd Edition. MIT Press, Cambridge, MA, USA.

Tura, A., HajNasser, Y., Keys, B. and Brown, L., 2013. Seismic detection of fractures from injection illustrated through a field example. The Leading Edge.

van Genuchten, M.T., 1980. A closed-form equation for predicting the hydraulic conductivity of unsaturated soils, Soil Sci. Soc. Am. J., 44(5), 892–898.

Virieux, J., 1986. P-sv wave propagation in heterogeneous media: Velocity-stress finite-difference method. Geophysics 51(4), 889–901. URL http://library.seg.org/doi/abs/10.1190/1.1442147

Virieux, J., Madariaga, R., 1982. Dynamic faulting studied by a finite difference method. Bulletin of the Seismological Society of America 72(2), 345–369. URL http://www.bssaonline.org/content/72/2/345.abstract

Wong, J., Bregman, N., West, G., Hurley, P., 1987. Crosshole seismic scanning and tomography. The Leading Edge 6(1), 36–41. URL https://doi.org/10.1190/1.1439327

Zhang, R., D. Vasco, T.M. Daley, and W. Harbert, 2015. Characterization of a fracture zone using seismic attributes at the In Salah CO_2 storage project. Interpretation, 3(2): SM37-SM46.

Zhang, Rui, Andrea Borgia, Thomas M Daley, Curtis M. Oldenburg, Yoojin Jung, Kyung Jae Lee, Tieyuan Zhu, Christine Doughty, Bilgin Altundas, Nikita Chugunov, T.S. Ramakrishnan, Time-lapse multi-scale seismic modeling of injected CO_2 in a fault zone for enhanced characterization of permeable flow paths in geothermal systems, in prep.

Zhang, Y. and G. Pinder, 2003. Latin hypercube lattice sample selection strategy for correlated random hydraulic conductivity fields, Water Resour. Res., 39(8), 1226. doi: 10.1029/2002WR001822.

Zhu, T., Harris, J., and Biondi, B. (2014). *Q*-compensated reverse-time migration, GEOPHYSICS, 79(3), S77-S87, doi.org/10.1190/geo2013-0344.1

This page left intentionally blank

13 APPENDIX I

Attach field test plan.

Conceptual Field Work Plan

Fault Identification and Characterization via Active Seismic Imaging of Injected CO_2 (ASCO)

Andrea Borgia, Thomas M. Daley, and Curtis M. Oldenburg
Energy Geosciences Division
Lawrence Berkeley National Laboratory

Introduction

Characterizing the transmissivity and connectivity of natural and stimulated faults and fractures is essential for the assessment and development of geothermal resources because it is the transmissive faults and fractures that provide both the actual surfaces for rock-fluid heat transfer and the pathway for fluid injection and production via geothermal wells. In fact, at most geothermal fields fluid is produced primarily from only one or a few highly permeable fractures or faults that intersect a geothermal well. Engineered localized fractures can be induced at enhance geothermal system (EGS) sites to provide hydraulic connection between conductive faults and fractures and producing wells (Genter et al., 2010). Geothermal reservoir development will certainly gain from the characterization of actual fracture and fault network geometry and their transmissive and heat transfer properties. The purpose of this document is to provide a conceptual field work plan for the testing and demonstration of a novel approach to characterize faults and fracture zones in geothermal reservoirs through the injection of carbon dioxide (CO_2) coupled with active seismic surveys and well logging.

Background

Carbon dioxide enhances the contrast in geophysical properties between fault/fractures and matrix for the following reasons:

1) CO_2 is non-wetting and will therefore tend to stay in the fault gouge without entering the pores of the intact rock matrix;
2) CO_2 is less viscous than formation brine, facilitating fault/fracture flow;
3) CO_2 is denser than other gases (like nitrogen or air) decreasing the upward buoyant flow of injected CO_2 that hampers recovery in vertical faults and fractures;
4) CO_2 is significantly more compressible than water at any given pressure/temperature condition, resulting in changes in the local stiffness tensor and corresponding seismic velocity.

A number of papers (Borgia et al., 2015, 2017a,b; Oldenburg et al., 2016; Lee et al., 2017; Zhang et al., 2017) show the theoretical advantages of injecting and producing supercritical CO_2 ($scCO_2$) in faults and fractures using push-pull well experiments for the purposes of improving the characterization of fault/fracture hydrological properties for a number of different fault/fracture topologies. In addition, the use of active-source geophysical monitoring and well logging allows the recording of the growth and shrinkage of the $scCO_2$ plume that, in turn, identifies the geometry of the transmissive zones of the fault/fracture.

Having demonstrated theoretically the possibility of improved fault/fracture geometry and property characterization by means of the active-seismic CO_2 (ASCO)-push-pull approach, the next step is to test this new methodology in a field experiment. In the following section, we list the characteristics that we envision are useful for making such an experiment a success.

Favorable Characteristics of Sites for CO_2 Push-Pull Injection and Monitoring

The optimal characteristics for a successful field test of ASCO are summarized in Table 1 that lists across the columns the four potential sites (Brady's, Desert Peak, San Emidio, and Dixie Valley shown located in Fig. 1 and along the rows the key properties for choosing the most promising of them. We also include the Sanford Underground Research Facility (SURF) as a possible site for comparison purposes.

Table 1. Potential sites for developing the ASCO experiment. Highlighted: yellow → best; green → good.

Properties ↓ **Locations** →	Brady's	Desert Peak	San Emidio	Dixie Valley	SURF
Depth of fault intersections	500-2000	500-2000	500-1500	500-1500	1478
Temperature °C	160-180	200-230	140-160	230-250	35
Lithology	metasediments	metasediments	metasediments	metasediments	phyllite and amphibolite
Known transmissive faults	yes	yes	yes	yes	no
Gouge or damage present	good	good	good	good	no
Open fractures within fault	very good	good	excellent	good	no
Sealed system	poorly	good	poorly	poorly	yes
Complexity of structures	complex	relatively simple	highly complex	complex	yes
wells geometry for seismic monitoring	excelent	very good	good	probably good	
Wells intersecting faults	yes	yes	yes	yes	not known currently
Availability of wells	probably many	good	probably few	probably few	numerous
Partnering potential	good	good	very good	very good	excellent
Degree of characterization	very good	very good	very good	very good	very good

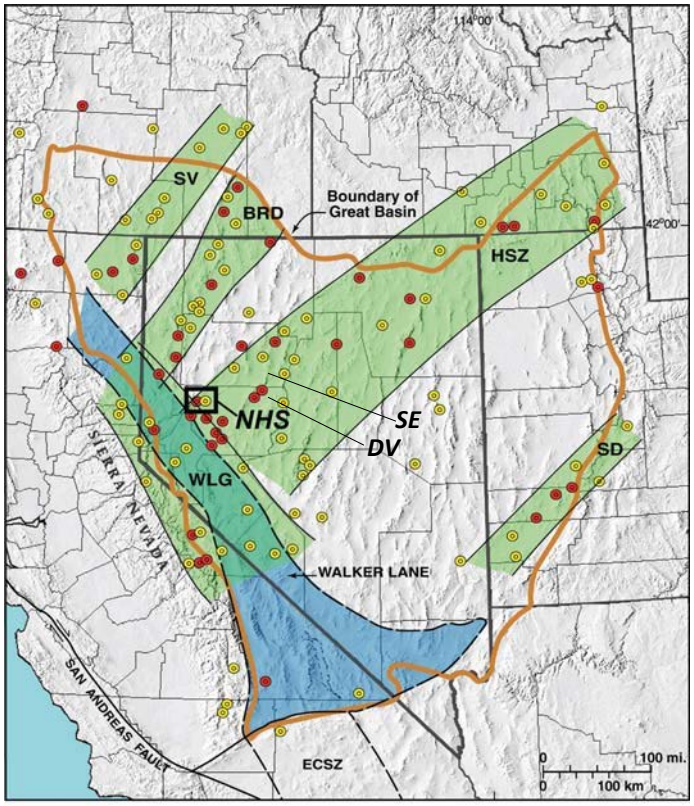

Fig. 1. Map of Nevada and the major sites of geothermal areas (after Faulds et al., 2010). ***NHS*** *is the Northern Hot Springs Mountains, where the Brady's and Desert Peak geothermal fields are located;* ***DV*** *is Dixie Valley;* ***SH*** *is San Emidio. Other geothermal belts:* ***SV*** *is Surprise Valley;* ***BRD*** *is Black Rock Desert;* ***HSZ*** *is Humboldt Structural Zone;* ***WLG*** *is Walker Lane;* ***SD*** *is Sevier Desert;* ***ECSZ*** *is Eastern California shear zone.*

Generally, the most important parameter for a first test of our methodology is the simplicity of the geological/structural setting. Ideally, we would like to have an already well-constrained, single, sub-vertical fault with a thick permeable fault gouge located between 2000 and 1000 m below the surface. The need for simplicity and an already-well-constrained fault system is obvious, because we need to test the results not only of the push-pull experiment but also of the inversion of the active seismic data. The depth is relevant in order to reduce to a minimum the buoyant rise of the injected $scCO_2$ to allow a wider permeation of the fault gouge. Toward this goal, it is also important that the fault be as much as possible sealed toward the surface. In practice, there should be no surface manifestation of the geothermal field to demonstrate the sealing capacity of the reservoir.

One other important aspect is the well geometry. We need a usable injection/production well that intersects the fault at the desired maximum depth. Because vertical seismic profiling (VSP) and crosswell seismic imaging appear to be the most promising techniques, additional wells are needed that would be used for the active-seismic monitoring of the growth and shrinkage of the $scCO_2$ plume. There should be at least one monitoring well on each side of the fault, near to in-

plane with the injection/production well and at an adequate separation. Actual locations would be dependent on site-specific modeling.

All of these characteristics, with different degrees of approximation to the optimum, are found in the Basin and Range geothermal fields. In the above table we have summarized four of them (Brady's, Desert Peak, San Emidio, and Dixie Valley geothermal fields) in addition to the SURF site. From the table, one may see that the Brady's and Dixie Valley geothermal fields have relatively more complex structures with normal and conjugate fault systems. San Emidio instead has faults that apparently have very large permeabilities with significant fault openings in addition to being directly vented at the surface. Therefore, it appears that the Desert Peak geothermal field is the most promising site, although the others may be considered as well at a later stage.

The Desert Peak Geothermal Field

The Desert Peak Geothermal Field in northern Nevada (Fig.1) is located in the Basin and Range Tectonic Province along the N-NE striking Rhyolite Ridge normal fault system (Faulds and Garside, 2003; Fauds et al., 2010 and 2012). The fault system (Fig. 1) is characterized by two large overlapping faults with multiple fault segments within the relay zone containing abundant bends. Slip on these segments may be responsible for stress concentrations and increased fracture density around the areas where productive wells are. The hydrothermal system is sealed and has no active surface hot springs or fumaroles (Benoit et al., 2006; Kratt et al., 2006; Faulds and Garside, 2003). Lutz et al. (2009) give a geological characterization of well data, Robertson-Tait et al. (2004), Davatzes and Hickman (2009), and Hickman and Davatzes (2010) present geomechanical analysis of wells, while rock mechanical analysis of representative core is given in Lutz et al. (2010). Additional data on reservoir behavior are derived from pressure interference tests (Zemach et al., 2010), tracer studies (Rose et al., 2010), and local seismic monitoring (Nathwani et al., 2011). Nevertheless, more work needs to be done to better constrain where and why geothermal activity concentrates only in some segments of this and other fault zones of the Basin and Range. Enhanced knowledge of such structures would facilitate exploratory drilling in known fault zones, including as yet untested areas where blind geothermal systems may possibly exist. In fact, regional analyses suggest that the majority of the geothermal resources in the Great Basin could be blind (Coolbaugh et al., 2007; Williams et al., 2009).

Conceptual Test Plan for ASCO at Desert Peak

Faulds et al. (2012) show a highly detailed geological, stratigraphic, and structural map of the Rhyolite Ridge Fault Zone within the Desert Peak Geothermal Field (Fig. 2) with a number of potential wells that could be used for the ASCO field test. The most obvious one of them is Well 22-22, which was actually used as a case study for our 2D and 3D numerical simulation of $scCO_2$ injection and production experiments (Borgia et al., in preparation) combined with synthetic active seismic fault imaging (Zhang et al., in preparation). Well B21-2 and B23-1 could complete the triplet. One other injection/production well could perhaps be 77-21, and wells ST-10 and 15 to complete the triplet for seismic imaging. In both of these cases we should inject $scCO_2$ at the easternmost of the three-step-over faults system that intersects the well deeper than 1000 m depth.

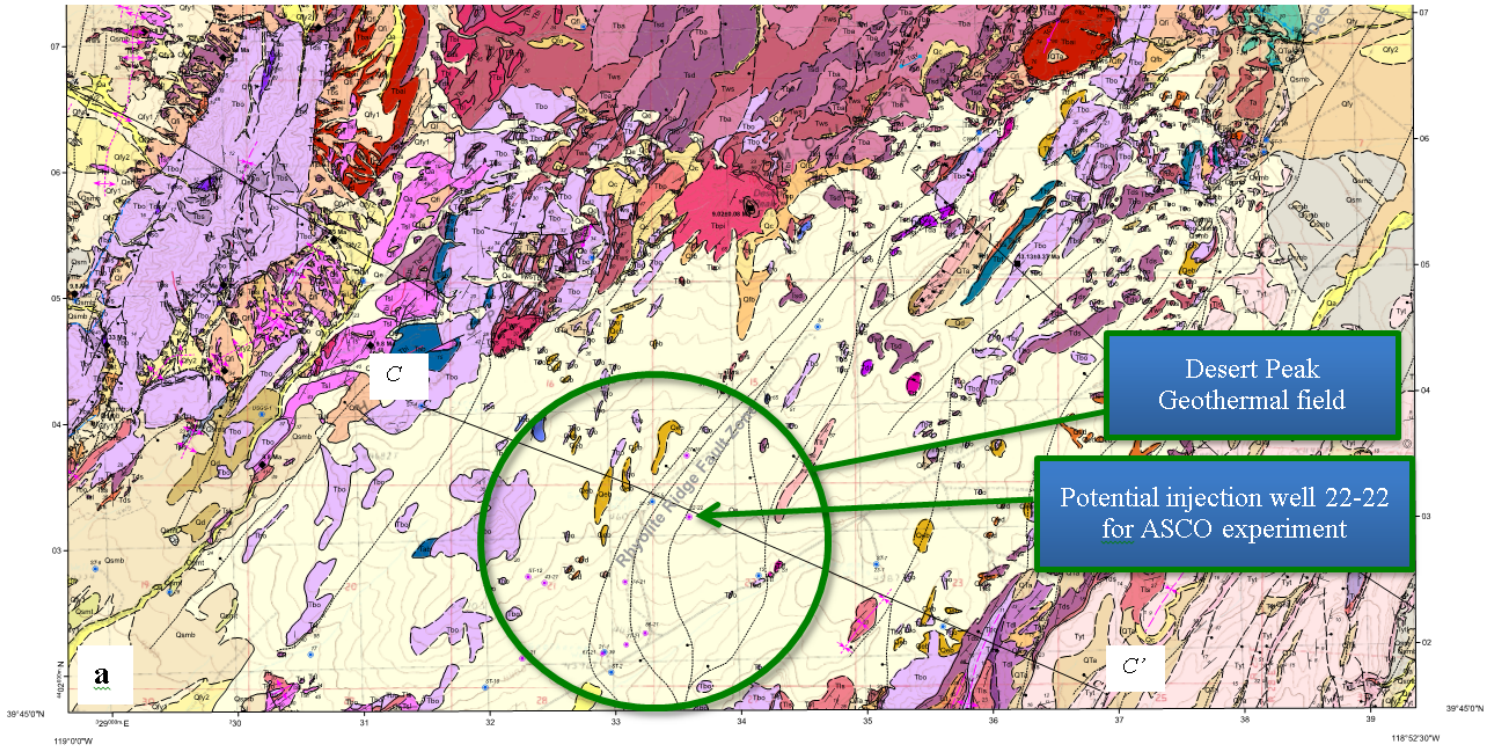
Desert Peak
Geothermal field
Potential injection well 22-22
for ASCO experiment
C
C'
a
Rhyolite Ridge Fault Zone

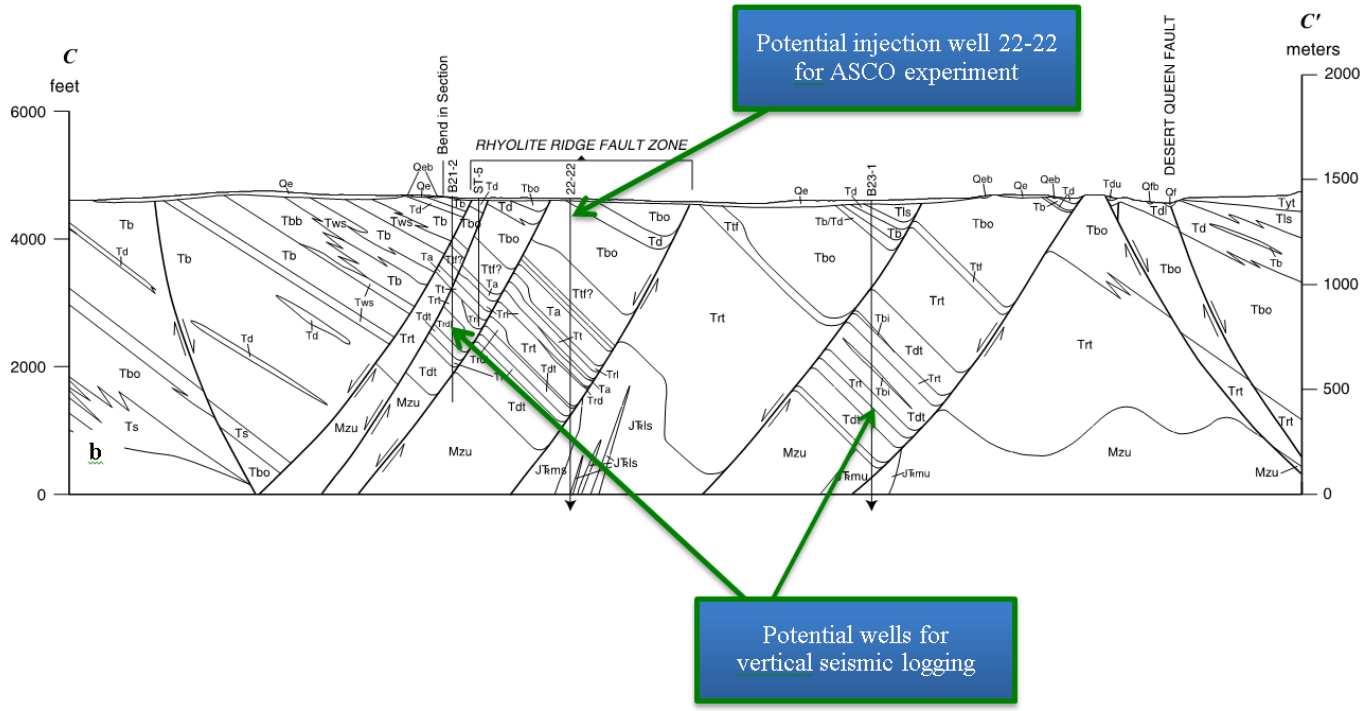

Fig. 2. Preliminary Geologic Map (a) and cross section (b) of the Desert Peak Geothermal Field, Desert County Nevada. We have indicated potential wells for the ASCO experiment along the cross section; there are, however, other arrangements that could be found more suitable following appropriate investigations. After Faulds et al., 2012 (see this paper for description of geologic units).

A tentative schedule to develop a test field site for ASCO is given in Table 2.

Table 2. *Schedule for ASCO field test development.*

Activity ↓ / Months into project →	2	4	6	8	10	12	14	16	18	20	22	24
In-depth analysis of potential sites for ASCO	■	■										
Contacting geothermal companies for interest	■	■										
Planning the experiment	■	■	■	■	■							
Field deployment of equipment					■	■						
Field testing of equipment						■	■					
Preliminary numerical simulations			■	■	■	■						
Running the experiment							■	■	■			
Numerical simulations, data analysis								■	■	■	■	
Writing reports, scientific papers									■	■	■	■
Conferences			■		■				■		■	■

Geophysical Monitoring

Following the assessment of potential sites, the field test design will be finalized during an initial planning phase (Table 2), which will include design of geophysical monitoring (seismic and well logging). Our initial concept for the field test is based on use of high-resolution borehole geophysics, including well logging, VSP, and crosswell seismic monitoring. Our optimal experiment would have four wells as shown in Fig. 3. Two wells would be perforated and open for fluid injection/withdrawal. The first would be a fault/fracture zone injection well with deeper perforated zone, and the second would be a geochemical sampling well with shallower perforated zone up-dip from the injection well. Two dedicated geophysical monitoring wells would be located about 30-50 m from the injection zone to allow high-resolution crosswell seismic imaging and VSP. All wells would also be used for well logging. The monitoring wells would be instrumented with fiber optic cables to allow for lower cost repeat-VSP using distributed acoustic sensing (DAS) (Daley, et al, 2016). The crosswell seismic could either be a wireline deployed, one-at-a-time crosswell survey or a sparser (fewer source-sensors) crosswell CASSM (continuous active-source seismic monitoring) (Daley, et al, 2006) experiment. In either case, the one monitor well would have seismic sources and the other would have seismic

sensors. An example of the crosswell source-sensor deployment is shown in Fig. 4, which has about 100 m vertical extent and 30 m well spacing. One control on the spatial resolution is the spacing of sources and sensors. As seen in Fig. 4, the sources have sparser sampling and ”gaps” in raypath coverage are visible, while the denser sensor sampling has smaller gaps. In a CASSM system, sparser coverage would be accepted for the much higher precision (and sensitivity) allowed. Optimizing the source-sensor sampling in terms of cost/benefit analysis would be part of the survey test design in the planning phase. For a wireline crosswell survey, multiple surveys would be planned with an initial four surveys suggested – one pre-injection characterization, one pre-injection baseline, one mid-injection, and one post-injection. The characterization survey would be used to decide final parameters to use in the following three surveys. Similarly, three VSP surveys and three well logging surveys would be planned corresponding to baseline, mid-injection and post-injection times.

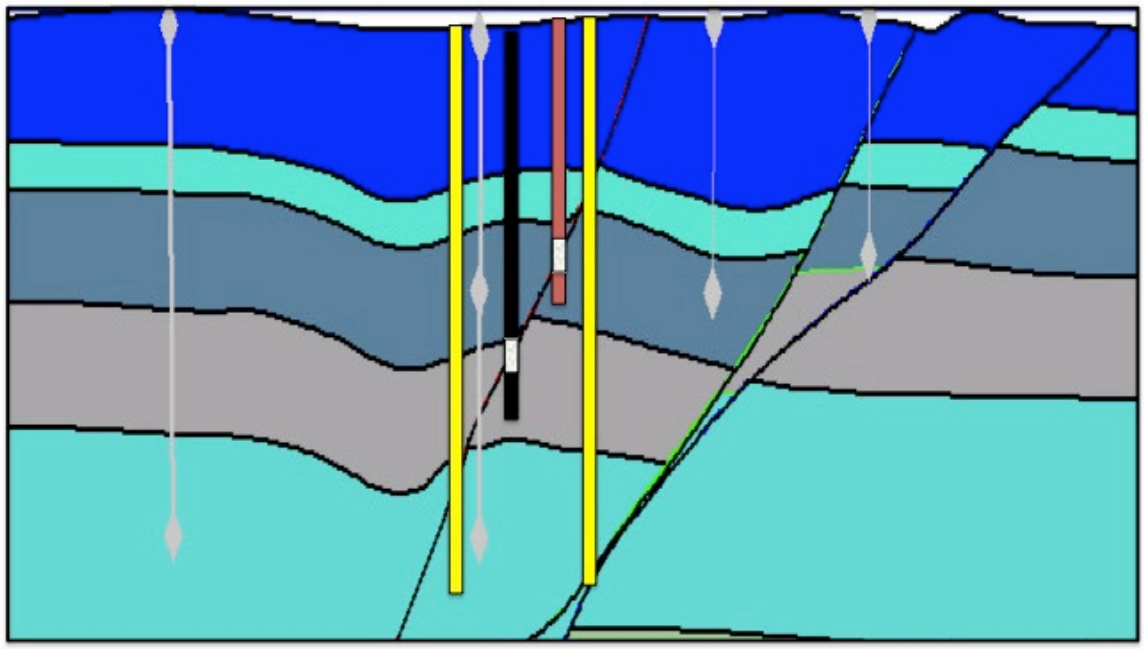

Fig. 3. Proposed fault experiment borehole geometry. The black borehole is an injection well perforated in the white interval, and the red borehole is a geochemical sampling well perforated in the white interval. The yellow wells are dedicated geophysical monitoring wells. The monitoring well spacing would ideally be 30-50 m from the injection well.

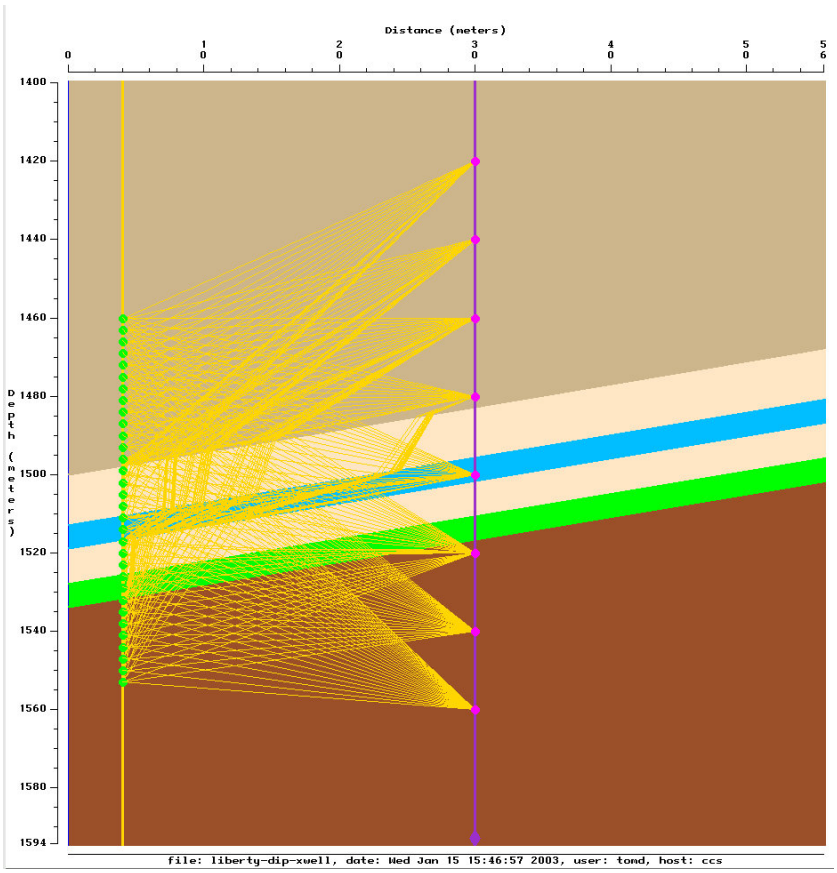

Fig. 4. Example crosswell seismic geometry and raypaths (yellow). The seismic source location are indicated by purple dots while the seismic sensor locations are green dots.

One key parameter to be designed via modeling in the early stages of the project is the amount of CO_2 required. For this particular experiment, a reasonable amount corresponds to a fault rock volume of 160 m upward dip x 125 m along strike x 10 m of gouge thickness. Thus, if the connected porosity of the fault gouge is 0.1 we need to fill with $scCO_2$ a volume of 20,000 m^3 at 7-10 MPa with a 50% CO_2-saturation, which is about 2,000 tons of CO_2. This volume, given a typical cost of $100-200 per ton, would require about one hundred deliveries with a 20-ton-capacity CO_2 truck over a period of about 60 days utilizing an on-site storage tank. As part of the planning phase, we would need to identify a source and cost of CO_2, both of which will constrain the volumes injected and thus the specifics of the monitoring design.

Conclusions

We have shown that use of $scCO_2$ has potential to enhance the imaging and characterization of transmissive fault and fracture networks in a geothermal reservoir. Improving the characterization of fault/fracture hydrological properties for a number of different topologies can be accomplished with push-pull type hydrologic testing and analysis. The spatial imaging of these topologies is best accomplished with high-resolution borehole geophysics in VSP and crosswell geometries. We have developed an initial field test plan to utilize these geophysical and well-test tools at an existing geothermal field.

Cited References

Benoit W.R., Hiner J.E., and Forest R.T., 1982. Discovery and geology of the Desert Peak geothermal field: A case history: Nevada Bureau of Mines and Geology Bulletin, v. 97, p. 82.

Borgia A., Oldenburg C.M., Zhang R., Pan L., Finsterle S., Ramakrishnan T.S., 2015. Simulations of CO2 push-pull in fractures to enhance geophysical contrast for characterizing EGS sites. PROCEEDINGS, TOUGH Symposium 2015, Lawrence Berkeley National Laboratory, Berkeley, California, September 28-30, p. 109-115.

Borgia A., Oldenburg C.M., Zhang R., Jung Y., Lee K.J., Doughty C., Daley T.M., Altundas B., Chugunov N., Ramakrishnan T.S., 2017a. Simulations of Carbon Dioxide Injection, Seismic Monitoring, and Well Logging for Enhanced Characterization of Faults in Geothermal Systems. PROCEEDINGS, 42nd Workshop on Geothermal Reservoir Engineering Stanford University, Stanford, California, February 13-15, SGP-TR-212.

Borgia A., Oldenburg C.M., Zhang R., Pan L., Daley T.M., Finsterle S., Ramakrishnan T.S., 2017b. Simulation of CO2 injection into fractures and faults for improving their geophysical characterization at EGS Sites. Geothermics, , v. 69, p. 189-201, http://dx.doi.org/10.1016/j.geothermics.2017.05.002.

Coolbaugh M.F., Sladek C., Faulds J.E., Zehner R.E., Oppliger G.L., 2007. Use of Rapid Temperature Measurements at a 2-Meter Depth to Augment Deeper Temperature Gradient Drilling. PROCEEDINGS: Thirty Second Workshop on Geothermal Reservoir Engineering, Stanford, California, January 22-24, 2007.

Daley T.M., Miller D.E., Dodds K., Cook P., Freifeld B.M., 2016. Field Testing of Modular Borehole Monitoring with Simultaneous Distributed Acoustic Sensing and Geophone Vertical Seismic Profile at Citronelle, Alabama. Geophysical Prospecting, v. 64 (5), p. 1318-1334, DOI: 10.1111/1365-2478.12324.

Daley T.M., Ajo-Franklin J.B., Christine D., 2011. Constraining the reservoir model of an injected CO_2 plume with crosswell CASSM at the Frio-II brine pilot. International Journal of Greenhouse Gas Control, v. 5, p. 1022-1030, DOI: 10.1016/j.ijggc.2011.03.002.

Daley, T.M., Solbau R.D., Ajo-Franklin J.B., Benson S.M., 2007. Continuous active-source monitoring of CO_2 injection in a brine aquifer. Geophysics, v. 72(5), p. A57–A61, DOI:10.1190/1.2754716.

Faulds, J.E., and Garside, L.J. 2003. Preliminary geologic map of the Desert Peak – Brady geothermal fields, Churchill County, Nevada, Nevada Bureau of Mines and Geology Open-File Report 03-27.

Faulds J.E., Coolbaugh M.F., Benoit D., Oppliger G., Perkins M., Moeck I., and Drakos P., 2010. Structural Controls of Geothermal Activitiy in the Northern Hot Spring Mountains, Western Nevada: The Tale of Three Geothermal Systems (Brady's, Desert Peak, and Desert Queen). GRC Transactions, v. 34, p. 675-683.

Faulds J.E., Ramelli A.R., Garside L.J., Coolbaugh M.F., and Green H.L., 2012. Preliminary Geologic Map of the Desert Peak Quadrangle, Churchil County, Nevada (US). Nevada Bureau Of Mines and Geology, Open-File Report 12-5.

Genter, A., Evans, K., Cuenot, N., Fritsch, D. and Sanjuan, B., 2010. Contribution of the exploration of deep crystalline fractured reservoir of Soultz to the knowledge of enhanced geothermal systems (EGS). Comptes Rendus Geoscience, v. 342(7), p. 502-516.

Jung Y., Doughty C., Borgia A., Lee K.J., Oldenburg C.M., Pan L., Daley T.M., Zhang R., Altundas B, Chugunov N., 2017. Pressure transient analysis during CO_2 push-pull tests into faults for EGS characterization, in prep.

Kratt C., Calvin W., and Coolbaugh M., 2006. Geothermal exploration with Hymap hyperspectral data at Brady-Desert Peak, Nevada. Remote Sensing of Environment, v. 104, p. 313-324.

Lee K.J., Oldenburg C.M., Doughty C., Jung Y., Borgia A., Pan L., Zhang R., Daley T.M., Altundas B, Chugunov N., 2017. Simulations of Carbon Dioxide Push-Pull into a Conjugate Fault System Modeled after Dixie Valley—Sensitivity Analysis of Significant Parameters and Uncertainty Prediction by Data-Worth Analysis, *Geothermics*, submitted.

Lutz S.J., Moore J.N., Jones C.G., Suemnicht G.A., and Robertson-Tait A., 2009. Geological and Structural Relationships in the Desert Peak Geothermal System, Nevada: Implications for EGS Development. PROCEEDINGS, Thirty-Fourth Workshop on Geothermal Reservoir Engineering, Stanford University, Stanford, California, February 9-11, 2009 SGP-TR-187.

Nathwani J., Majer E., Boyle K., Rock D., Peterson J. and Jarpe S., 2011. DOE real-time seismic monitoring at enhanced geothermal system sites. Thirty-sixth workshop on Geothermal Reservoir Engineering, SGP-TR- 191.

Rose p., Leecaster K., Drakos P., Rotertson-Tait A., 2009. Tracer Testing at the Desert Peak EGS Project. Geothermal Resources Council Transactions, v. 33.

Oldenburg, C.M., Daley, T.M., Borgia, A., Zhang, R., Doughty, C., Ramakrishnan, T.S., Altundas, B., Chugunov, N., 2016. Preliminary Simulations of Carbon Dioxide Injection and Geophysical Monitoring to Improve Imaging and Characterization of Faults and Fractures at EGS Sites. PROCEEDINGS, 41st Workshop on Geothermal Reservoir Engineering, Stanford University, Stanford, California, February 22-24, 2016, SGP-TR-209.

Williams C.F., Reed M.J., DeAngelo J., and Galanis S.P. Jr., 2009. Quantifying the undiscovered geothermal resources of the United States: Geothermal Resources Council Transactions, v. 33, p. 995-1002.

Zemach E., Drakos P., Robertson-Tait A., 2009. Feasibility Evaluation of an “in-field” EGS project at Desert Peak, Nevada. Geothermal Resources Council Transaction, v. 33, p. 285-295.